

# **Naval Surface Warfare Center Carderock Division**

West Bethesda, MD 20817-5700

---

**NSWCCD-50-TR-2004/010** December 2004

Hydromechanics Department Report

## **Performance of Propeller 4381 in Crashback**

by

Christopher J. Chesnakas

Martin J. Donnelly

David J. Fry

Stuart D. Jessup

Joel T. Park



---

Approved for public Release. Distribution unlimited.

---

# **Naval Surface Warfare Center**

## **Carderock Division**

West Bethesda, MD 20817-5700

---

**NSWCCD-50-TR-2004/010** December 2004

Hydromechanics Department Report

### **Performance of Propeller 4381 in Crashback**

by

Christopher J. Chesnakas

Martin J. Donnelly

David J. Fry

Stuart D. Jessup

Joel T. Park

---

Approved for public release. Distribution unlimited.

---

This page intentionally left blank.

# REPORT DOCUMENTATION PAGE

Form Approved  
OMB No. 0704-0188

Public reporting burden for this collection of information is estimated to average 1 hour per response, including the time for reviewing instructions, searching existing data sources, gathering and maintaining the data needed, and completing and reviewing this collection of information. Send comments regarding this burden estimate or any other aspect of this collection of information, including suggestions for reducing this burden to Department of Defense, Washington Headquarters Services, Directorate for Information Operations and Reports (0704-0188), 1215 Jefferson Davis Highway, Suite 1204, Arlington, VA 22202-4302. Respondents should be aware that notwithstanding any other provision of law, no person shall be subject to any penalty for failing to comply with a collection of information if it does not display a currently valid OMB control number. **PLEASE DO NOT RETURN YOUR FORM TO THE ABOVE ADDRESS.**

<b>1. REPORT DATE (DD-MM-YYYY)</b> 31-Dec-2004		<b>2. REPORT TYPE</b> Final		<b>3. DATES COVERED (From - To)</b> -	
<b>4. TITLE AND SUBTITLE</b>  Performance of Propeller 4381 in Crashback				<b>5a. CONTRACT NUMBER</b>	
				<b>5b. GRANT NUMBER</b>	
				<b>5c. PROGRAM ELEMENT NUMBER</b>	
<b>6. AUTHOR(S)</b>  Christopher J. Chesnakas, Martin J. Donnelly, David J. Fry, Stuart D. Jessup, and Joel T. Park				<b>5d. PROJECT NUMBER</b>	
				<b>5e. TASK NUMBER</b>	
				<b>5f. WORK UNIT NUMBER</b> 01-1-5400-105	
<b>7. PERFORMING ORGANIZATION NAME(S) AND ADDRESS(ES) AND ADDRESS(ES)</b>  Naval Surface Warfare Center Carderock Division 9500 Macarthur Boulevard West Bethesda, MD 20817-5700				<b>8. PERFORMING ORGANIZATION REPORT NUMBER</b>  NSWCCD-50-TR-2004/010	
<b>9. SPONSORING / MONITORING AGENCY NAME(S) AND ADDRESS(ES)</b>  Office of Naval Research (ONR) ATT: Dr. Ki-Han Kim, Code 333 Ballston Centre Tower One 800 North Quincy Street Arlington, VA 22217-5660				<b>10. SPONSOR/MONITOR'S ACRONYM(S)</b> ONR	
				<b>11. SPONSOR/MONITOR'S REPORT NUMBER(S)</b>	
<b>12. DISTRIBUTION / AVAILABILITY STATEMENT</b> Approved for public release. Distribution unlimited.					
<b>13. SUPPLEMENTARY NOTES</b>					
<b>14. ABSTRACT</b> Propeller operation in crashback is technically very challenging both computationally and experimentally. Propeller 4381 was evaluated experimentally in Carderock's 36-inch (0.91 m) water tunnel. Propeller 4381 was operated in the ahead condition for comparison. Details of the flowfield were measured with 3-component laser Doppler velocimetry (LDV) and 2-component particle imaging velocimetry (PIV). Propulsion performance was measured with thrust and torque transducers. Cavitation was documented photographically with a strobe light, and flow visualization was conducted with a vertical laser light sheet for observation of the recirculation region of the propeller in crashback. Highly random cavitation occurred on the propeller in crashback on the downstream side at the leading edge, which is the trailing edge for ahead. A highly unstable recirculation zone occurred with a ring vortex near the propeller tip. The maximum variation in thrust and torque as computed from the standard deviation relative to the mean load with a value of 0.25 occurred at an advance ratio of $J = -0.5$ . The high variation in loads appeared to correlate with the maximum total kinetic energy relative to tunnel velocity in the flow at the blade tip, which was measured by LDV as 1.5. These results indicate that vibration and wear may be reduced by minimizing operation near $J = -0.5$ for this propeller.					
<b>15. SUBJECT TERMS</b> crashback, cavitation, laser Doppler velocimetry, propeller, propulsion, tip vortex, ring vortex, propeller backing					
<b>16. SECURITY CLASSIFICATION OF:</b>			<b>17. LIMITATION OF ABSTRACT</b>  SAR	<b>18. NUMBER OF PAGES</b>  50	<b>19a. NAME OF RESPONSIBLE PERSON</b> Stuart D. Jessup, Ph. D.
<b>a. REPORT</b> UNCLASSIFIED	<b>b. ABSTRACT</b> UNCLASSIFIED	<b>c. THIS PAGE</b> UNCLASSIFIED			<b>19b. TELEPHONE NUMBER (include area code)</b> 301-227-5080

This page intentionally left blank.

## Contents

	<i>Page</i>
Abstract.....	1
Administrative Information .....	1
Acknowledgements.....	1
Introduction.....	2
Experimental Apparatus.....	3
Water Tunnel .....	3
Propeller.....	3
Dynamometer.....	3
Flow Visualization and Cavitation.....	3
Laser Doppler Velocimetry (LDV).....	4
System Description .....	4
Coordinate System for Experimental Results.....	4
Uncertainty Analysis.....	5
Test Conditions .....	6
Particle Imaging Velocimetry (PIV).....	6
Results.....	7
Dynamometer.....	7
Flow Visualization and Cavitation.....	8
Laser Doppler Velocimetry.....	9
Particle Imaging Velocimetry .....	11
Conclusions.....	12
References.....	49

## Figures

	<i>Page</i>
Figure 1. Propeller 4381 Geometry .....	15
Figure 2. Fiber-Optic Probes in the 36-inch Water Tunnel .....	15
Figure 3. Primary-Secondary Flow Coordinate System for LDV Measurements .....	16
Figure 4. Flow Vectors and Angles for LDV Measurements .....	16
Figure 5. PIV Experimental Arrangement in 36-inch Water Tunnel.....	17
Figure 6. Thrust and Torque Coefficients for Ahead Condition at 650 and 660 rpm.....	18

Figure 7. Thrust and Torque Coefficients for Crashback .....	18
Figure 8. Reynolds Number Effect on Crashback for Thrust & Torque at $J = -0.5$ .....	19
Figure 9. Reynolds Number Effect on Crashback for Thrust & Torque at $J = -0.7$ .....	19
Figure 10. Standard Deviation of Thrust in Ahead and Crashback .....	20
Figure 11. Standard Deviation of Torque in Ahead and Crashback .....	20
Figure 12. Signal to Noise Ratio for Thrust.....	21
Figure 13. Signal to Noise Ratio for Torque.....	21
Figure 14. Reynolds Number Effect on Standard Deviation of Thrust .....	22
Figure 15. Reynolds Number Effect on Standard Deviation of Torque .....	22
Figure 16. Laser Light Sheet Illumination of Vortex Ring for Propeller 4381 .....	23
Figure 17. Hub Vortex Cavitation of Propeller 4381 in Ahead Condition.....	24
Figure 18. Tip and Hub Cavitation for Propeller 4381 in Ahead Condition .....	24
Figure 19. Cavitation of Propeller 4381 in Crashback .....	25
Figure 20. Spanwise Circulation at $J = +0.3$ .....	26
Figure 21. Streamwise Velocity for P4381 from LDV at $J = +0.3$ , $x = +0.23$ .....	27
Figure 22. Blade Wake from LDV at $J = +0.3$ , $x = 0.7$ .....	28
Figure 23. Computed Drag Coefficients for P3381 at $J = +0.3$ & P4119, $J_{des} = 0.83$ .....	28
Figure 24. Local Total Kinetic Energy in Ahead for Propeller 4381 at $J = +0.3$ .....	29
Figure 25. Detail of Tip Vortex in Ahead at $J = +0.3$ .....	29
Figure 26. Local Total Kinetic Energy in Crashback for Prop 4381 at $J = -0.5$ .....	30
Figure 27. Local Total Kinetic Energy in Crashback for Prop 4381 at $J = -0.7$ .....	30
Figure 28. Streamwise Velocity in Crashback for Prop 4381 at $J = -0.5$ .....	31
Figure 29. Mean Velocity Components in Crashback at $J = -0.5$ .....	31
Figure 30. X-R Plane Total Kinetic Energy in Crashback at $J = -0.5$ .....	32
Figure 31. Mean Velocity Components in Crashback at $J = -0.7$ .....	32
Figure 32. X-R Plane Total Kinetic Energy in Crashback at $J = -0.7$ .....	33
Figure 33. Averaged Relative Velocities of Tip Vortex from PIV at $J = +0.3$ .....	35
Figure 34. Comparison of PIV and LDV Radial Velocity in Crashback at $J = -0.5$ .....	36
Figure 35. Comparison of PIV and LDV Axial Velocity in Crashback at $J = -0.5$ .....	37
Figure 36. Comparison of PIV and LDV Radial Velocity in Crashback at $J = -0.7$ .....	38
Figure 37. Comparison of PIV and LDV Axial Velocity in Crashback at $J = -0.7$ .....	39
Figure 38. Average Streamline Velocity from Mosaic of 6 PIV Images at $J = -0.7$ .....	40
Figure 39. Instantaneous Velocity Vectors from PIV in Crashback at $J = -0.5$ .....	41
Figure 40. Instantaneous Velocity Vectors from PIV in Crashback at $J = -0.7$ .....	42
Figure 41. Instantaneous Axial Velocity and Streamlines from PIV at $J = -0.5$ .....	44
Figure 42. Eight Most Extreme Propeller Inflow Axial Velocity Data .....	44
Figure 43. Average and “Extreme” Propeller 4381 Inflow from at $J = -0.5$ .....	45

## Tables

	<i>Page</i>
Table 1. Geometric Characteristics of Propeller 4381 .....	47
Table 2. Elemental Uncertainties for LDV Measurements.....	47
Table 3. Calculated Uncertainties for LDV Measurements.....	48
Table 4. Test Conditions .....	48
Table 5. Thrust and Torque Predictions at $J = +0.3$ .....	48
Table 6. Comparison of Propulsion and Flow Statistics.....	48

## Symbols

$C$	Propeller chord length
$C_d$	Drag coefficient
$d$	Wake momentum thickness
$D$	Propeller diameter
$f$	Maximum blade section camber
$G$	Circulation
$i$	Blade rake
$J$	Propeller advance coefficient, $U_\infty/nD$
$K_Q$	Torque coefficient, $Q/(\rho n^2 D^5)$
$K_T$	Thrust coefficient, $T/(\rho n^2 D^4)$
$n$	Propeller rotational speed, rev/s
$N_b$	Blade number
$P$	Propeller pitch
$q$	Root-mean-square (RMS) fluctuation of velocity, $\text{TKE} = q^2/2$ , normalized by $U_\infty$
$q^*$	Root-mean-square (RMS) fluctuation of velocity, normalized by $V_\infty$
$Q$	Torque
$r$	Radius or radial coordinate in cylindrical coordinate system, normalized by $R$
$R$	Propeller radius
$SNR$	Signal to noise ratio
$t$	Maximum blade section thickness or tangential coordinate for cylindrical coordinate system
$T$	Thrust
$U_r$	Radial velocity in the measured (fixed) frame, positive outward, normalized by $U_\infty$
$U_t$	Tangential velocity in the measured (fixed) frame, positive counterclockwise looking downstream, normalized by $U_\infty$
$U_x$	Axial velocity in the measured (fixed) frame, positive downstream, normalized by $U_\infty$
$U_\infty$	Inflow velocity in the stationary frame (i.e., tunnel velocity)
$V$	Total velocity in the rotating frame
$V_c$	Cross-stream velocity in the rotating frame, normalized by $U_\infty$
$V_r$	Radial velocity, normalized by $U_\infty$ (identical to $U_r$ )
$V_s$	Streamwise velocity in the rotating frame, normalized by $U_\infty$
$V^*$	Streamwise velocity in the rotating frame, normalized by $V_\infty$

$V_t$	Tangential velocity in the rotating frame, positive counterclockwise looking downstream, normalized by $U_\infty$
$V_x$	Axial velocity, normalized by $U_\infty$ (identical to $U_x$ )
$V_\theta$	Secondary velocity magnitude $(V_c^2 + V_r^2)^{1/2}$
$V_\infty$	Inflow velocity in the rotating frame $(U_\infty^2 + (2\pi rn)^2)^{1/2}$
$x$	Axial coordinate from propeller mid plane normalized by $R$
$y$	Vertical coordinate from shaft centerline normalized by $R$
$z$	Lateral coordinate from shaft centerline normalized by $R$
$\eta$	Propeller efficiency, $\frac{J}{2\pi} \frac{K_T}{K_Q} = \frac{U_\infty T}{\omega Q}$
$\theta$	Circumferential angle, radians
$\theta_s$	Blade skew angle
$\rho$	Density
$\sigma_x$	Standard deviation of $x$
$\tau$	Time
$\phi$	Propeller pitch angle
$\omega$	Propeller rotational speed, $2\pi n$ , rad/s

## **Abstract**

Propeller operation in crashback is technically very challenging both computationally and experimentally. Propeller 4381 was evaluated experimentally in Carderock's 36-inch (0.91 m) water tunnel. Propeller 4381 was operated in the ahead condition for comparison. Details of the flowfield were measured with 3-component laser Doppler velocimetry (LDV) and 2-component particle imaging velocimetry (PIV). Propulsion performance was measured with thrust and torque transducers. Cavitation was documented photographically with a strobe light, and flow visualization was conducted with a vertical laser light sheet for observation of the recirculation region of the propeller in crashback. Highly random cavitation occurred on the propeller in crashback on the downstream side at the leading edge, which is the trailing edge for ahead. A highly unstable recirculation zone occurred with a ring vortex near the propeller tip. The maximum variation in thrust and torque as computed from the standard deviation relative to the mean load with a value of 0.25 occurred at an advance ratio of  $J = -0.5$ . The high variation in loads appeared to correlate with the maximum total kinetic energy relative to tunnel velocity in the flow at the blade tip, which was measured by LDV as 1.5. These results indicate that vibration and wear may be reduced by minimizing operation near  $J = -0.5$  for this propeller.

## **Administrative Information**

The work described in this report was performed by the Propulsion and Fluid Systems Department (Code 54) of the Hydromechanics Directorate at the Naval Surface Warfare Center, Carderock Division (NSWCCD) in West Bethesda, Maryland. The work was funded by the Office of Naval Research, Code 333, as part of the FY01 6.2 Advanced Propulsor Program managed by Dr. Ki-Han Kim under Program Element 0602121N. The work was performed under work unit 01-1-5400-105.

## **Acknowledgements**

The co-authors are acknowledged individually for all the contributing efforts encompassing this work. Chris Chesnakas conducted the LDV measurements. Dave Fry conducted the PIV measurements. Martin Donnelly conducted load measurements. Joel Park prepared the NSWCCD report on the work, and Scott Black performed the Crashback analysis using the panel code. Supporting panel calculations were provided by Thad Michael.

## Introduction

The crashback condition is one of the most complex and challenging propeller operating conditions to analyze. For this report, crashback is defined as steady forward motion (ahead condition) with the propeller rotating in reverse. The advance ratio,  $J$ , for the propeller is then negative. The fluid mechanics of crashback is dominated by the interaction of the free stream flow field with strong recirculation driven by the local propeller induced velocity pushing fluid forward against the incoming free stream flow. Extreme flow unsteadiness directly coupled to varying degrees of blade surface flow separation make computations of forces extremely difficult.

A more fundamental understanding of crashback is necessary for improved ship operation and propeller maintenance. Service life of propellers may be extended. Additionally, an improved understanding can support maneuvering.

Jiang et al. [1] documented the unsteady ring vortex structure with particle imaging velocimetry (PIV) and related the unsteadiness to the measured unsteady shaft forces. Jiang identified an oscillation of the ring vortex at a frequency much lower than the propeller rotation rate.

RANS (Reynolds averaged Navier-Stokes) computations have shown large discrepancies with open water data, which Chen [2] attributed to effects of cavitation. Viscous effects and extremely large propeller inductions of the blade flow, which result in attached tip flow while the root region exhibited separated flow. The results from Chen [2] show the mean flow field in the axial plane with a ring vortex visualized outboard of the tip. Chen modeled only a single blade passage, thus assuming blade periodic flow. This assumption precludes simulating the time varying, spatially non-uniform flow field, and can only simulate unsteadiness within a blade passage.

Unsteady RANS was applied to the motion simulation of a submarine in a crashback maneuver, as reported by Davoudzadeh, et al. [3]. A full simulation of the entire submarine body and rotating propeller was performed during which the propeller direction of rotation was reversed. All the propeller blades were modeled separately to capture the unsteady flow field within the entire propeller disk. The flow field was analyzed in the vicinity of the propeller showing the unstable character of the vortex ring structure. Unfortunately, the computation was not validated with any experimental data.

CFD (computational fluid dynamics) validation for the crashback condition requires steady and unsteady data including measurements of the near-propeller flow field, blade surface flow, net shaft forces, and individual blade thrust and torque. LDV (laser Doppler velocimetry) measurements can capture the time average flow. The unsteady flow, being non-periodic, requires instantaneous velocity measurement techniques, such as PIV (particle imaging velocimetry). This report documents some of the experimental data necessary for CFD validation. The measurements include the following: propeller shaft loads, LDV, PIV, cavitation, and laser sheet visualization.

## **Experimental Apparatus**

### **Water Tunnel**

All measurements were made in the David Taylor, 36-inch (0.91 m), Variable Pressure Water Tunnel. The tunnel is a recirculating design with interchangeable test sections. A 36-inch (0.91 m) diameter, open-jet test section was used for these tests. The tunnel allows the pressure in the test section to be varied so that cavitation inception can be investigated. Both upstream and downstream drives are available for propeller testing. For these tests, the propeller was driven from upstream. Inflow to the propeller was uniform except for the wakes from the three upstream shaft support struts and the hub boundary layer from the upstream shaft. The flow geometry is similar to that of many surface ship designs.

### **Propeller**

The propeller used for this investigation is the David Taylor Propeller 4381. This is a five-bladed, 305 mm (12.0-inch) diameter, right-handed propeller with no skew and rake. Geometric characteristics of the propeller are listed in Table 1 and shown in Figure 1. This propeller was also used in the crashback studies described in the Introduction [2], [3].

### **Dynamometer**

Loads were measured with 36-inch Water Tunnel Standard Dynamometer #5, which contains two sets of strain gage bridges each for thrust and torque for a total of 4. The full range of the dynamometer is 16,000 N (3,600 lb) of thrust and 1,220 N-m (900 ft-lbs) of torque. The dynamometer was calibrated for both sets of sensors over the ranges of  $\pm 10,700$  N (2,400 lbs) in thrust and  $\pm 813$  N-m (600 ft-lbs) in torque. Tunnel velocity was calculated via a differential pressure measurement through the contraction with a correction factor based upon an LDV survey in an empty test section. The gage for this measurement was a Viatran Model 274 with a full-scale range of 103 kPa (15 psi) and an accuracy of  $\pm 0.15\%$  full scale. The velocity range of the experiments was 0.76 to 3 m/s (2.5 to 9.8 ft/s) while the rotational rate of the dynamometer was between 500 and 800 rpm. Both ahead and crashback data were acquired. Data acquisition and analysis system was based on National Instruments hardware a PXI-1000B rack, PXI-8170 embedded computer, and a PXI-6031E multi-function I/O device with 16 bit A/D resolution. Software and data reduction routines were written in LabVIEW v6.1.

### **Flow Visualization and Cavitation**

Light for the flow visualization came from an argon-ion laser producing 5 watts of power on all lines. The light was coupled into a multimode optical fiber to direct the light to the test section. The light sheet was generated using a cylindrical lens assembly at the fiber output end. The light sheet had a divergence angle of approximately  $7.5^\circ$  in water, and a sheet thickness of approximately 10 mm (0.4 inches). The light was projected through the upper diagonal window of the test section with the plane of the light sheet containing the propeller axis. The camera viewed the sheet through the opposite upper diagonal window, so that the image direction was perpendicular to the light sheet. The camera recorded images of cavitation bubbles passing through the light sheet.

Cavitation observations were performed with strobe-light illumination in the typical fashion. Recording was performed with a Sony Digital Betacam broadcast quality video camera/recorder. Still images of the cavitation were downloaded from the video to JPG files using an AVID editing system. In crashback, the cavitation and flow visualization experiments were conducted at tunnel pressures of 83, 110, and 138 kPa (12, 16, and 20 psia).

## Laser Doppler Velocimetry (LDV)

### *System Description*

The LDV system consisted of two TSI model 9832 fiber optic probes rigidly mounted together on a traverse, which could translate in the axial and radial directions as shown in Figure 2. The focal distance of the probes (470 mm in water) was sufficient to place the probe bodies outside of the jet. The horizontal probe utilized the green (514.5 nm) and violet (476 nm) beams of an argon-ion laser to measure the tangential and axial components of velocity, respectively. The vertical probe utilized the blue (488 nm) beam of the argon-ion laser to measure the radial component of velocity. Both probe volumes were 0.07 by 1.3 mm.

The measurement volume was positioned at a point in the horizontal plane containing the propeller axis. The probe volume was translated in the axial and radial directions in order to get two directions of movement in the flow field, while the rotation of the propeller relative to the measurement point provided the third direction of movement. The position of the shaft was encoded with an 8192-counts/revolution signal, which was recorded with each velocity measurement. The measurements are grouped into 1024 circumferential positions, each 8 encoder counts wide.

Doppler signals were analyzed with a TSI Model IFA 655 Digital Burst Correlator. The processor performs a 256-sample, double-clipped, autocorrelation on each Doppler burst, allowing the measurement of velocity even when the signal-to-noise ratio is low. The processors were operated in the random mode.

The flow was seeded with 1500 grit silicon-carbide powder with particles 1 to 2  $\mu\text{m}$  in size. Since the water in the tunnel recirculates, seed particles needed to be added only infrequently.

### *Coordinate System for Experimental Results*

All length scales presented here are normalized by the propeller radius,  $R$ , while the velocity measurements are generally normalized by the tunnel velocity,  $U_\infty$ . The exception to this are velocities with a superscript asterisk, which are normalized by the *relative* inflow velocity

$$V_\infty = \sqrt{U_\infty^2 + (2\pi r n)^2} \quad (1)$$

Measurements of the circumferentially averaged velocities are presented in the stationary coordinate system, while the velocity planes are presented in the rotating coordinate system of the blades. In order to better illustrate the features of the flow, the velocities in the downstream measurement planes are rotated into the primary-secondary coordinate system shown Figure 3. In this coordinate system, a primary, or streamwise, direction  $\mathbf{s}$  is defined by the propeller pitch angle,  $\phi$ , and the radial flow angle,  $\psi$ . The perpendicular direction  $\mathbf{p}$  is in the  $x$ - $r$  plane at  $\psi$  to the  $r$  axis, and the cross-stream direction  $\mathbf{c}$  is perpendicular to both  $\mathbf{s}$  and  $\mathbf{p}$ , forming a right-hand  $s$ - $c$ -

$p$  system. The  $x$ - $t$ - $r$  velocity components can be converted to the primary-secondary coordinate system using

$$\begin{aligned} V_s &= \sin \phi \cos \psi \cdot V_x + \cos \phi \cdot V_t + \sin \phi \sin \psi \cdot V_r \\ V_c &= -\cos \phi \cos \psi \cdot V_x + \sin \phi \cdot V_t - \cos \phi \sin \psi \cdot V_r \\ V_p &= -\sin \psi \cdot V_x - \cos \psi \cdot V_r \end{aligned} \quad (2)$$

For a given radial position, the pitch angle of the propeller at that radius is used. If the radius is inboard of the propeller root or outboard of the propeller tip,  $\phi$  is defined by the root or tip  $P/D$ , respectively. The flow vector in the stationary frame,  $U$ , and the flow vector in the rotating frame,  $V$ , are related by

$$V_x = U_x, \quad V_t = U_t - 2\pi r n, \quad V_r = U_r \quad (3)$$

The relations between the flow vectors, the propeller pitch angle,  $\phi$ , the flow angle,  $\beta$ , and the relative flow angle,  $\alpha$ , are all illustrated in Figure 4.

### Uncertainty Analysis

The uncertainties for the fundamental quantities measured in this experiment are listed in Table 2. Those uncertainties, which are the same for all measurements, are listed as Type B uncertainties, and those uncertainties, which vary for each measurement, are listed as Type A uncertainties per the ISO Uncertainty Guide [4]. Uncertainties are listed as a fraction of the nominal value, unless otherwise noted.

The uncertainties in  $x$ ,  $t$ , and  $r$  are the uncertainties in positioning the probe volume with respect to the propeller in the axial, tangential, and radial directions. Uncertainty in the measurement of the frequency is assumed to be small relative to the uncertainty due to finite sample size, and so is ignored. The uncertainty in the perpendicularity of the three measured components is assumed to be small compared to the uncertainty in fringe spacing and probe volume coincidence, and is ignored as well.

The calculated uncertainties for the quantities found by combining other measurements are presented in Table 3. The calculation of the uncertainty in  $J$  from the uncertainties in Table 2 is straightforward. However, the rest of the items in Table 3 can only be calculated with information on the local flow conditions. This is because all of these items depend on the values of the velocity, velocity gradients, or turbulence intensity. The uncertainties in Table 3 are therefore listed for two representative flow conditions. The first, case 1, is a point in the “inviscid” flow between the blade wakes. In this region, the turbulence intensity is low and the flow gradients are small. Case 1 is representative of the majority of the flow. Case 2 is a point in the blade wake. At this location, the turbulence intensity and the velocity gradients are at their highest values, and so the uncertainties are a maximum. Case 2 is representative of only a very small fraction of the flow, but the fraction of most interest.

For case 1, the velocity uncertainties are all below 0.5% of the inflow velocity. In this region of the flow, the velocity uncertainty is dominated by the uncertainty in the fringe spacing of 0.3. For case 2, the uncertainties are higher due to the uncertainty in finding the mean in a high turbulence region with a relatively small sample size ( $\sim 250$ ). Type A uncertainty in the measurement of the turbulent velocity fluctuations,  $q$ , is dominated by the uncertainty in finding the variance of a distribution with a finite sample size. For a sample size of 250, that uncertainty

is approximately 10%. The LDV has a lower noise floor, below which it cannot measure the turbulence. For this setup, the noise floor in  $q$  was approximately 1.5% of the measured velocity.

### ***Test Conditions***

Measurements were performed in the ahead condition at  $J = +0.3$ , and in crashback at both  $J = -0.5$  and  $-0.7$ . The  $J = +0.3$  condition represented a bollard condition in the water. This was the lowest  $J$  obtainable, due to flow recirculation in the water tunnel. At all advance coefficients, planes perpendicular to the axis were measured ahead of and behind the propeller. At the crashback conditions,  $x$ - $r$  planes containing the shaft axis were also measured. In order to obtain the best LDV measurements, the propeller was operated at conditions for which cavitation was suppressed, typically 241 kPa (35 psia) for  $J = +0.3$  and 345 kPa (50 psia) in crashback. The test conditions for LDV and PIV are summarized in Table 4.

### **Particle Imaging Velocimetry (PIV)**

The PIV measurements were made using two Spectra Physics Quanta-Ray PRO-Series Pulsed Nd:YAG lasers rated at 800-mJ/pulse output at 532 nm. The laser output was formed into a light sheet of 5-mm thickness. The light sheet passed through windows in the water tunnel to illuminate the flow. The sheet was oriented horizontally, parallel to the propeller-shaft axis shown in Figure 5. The axial position of the camera and sheet were moved to place the blade center span in the center of the image. Silicon Carbide particles of mean diameter 1  $\mu\text{m}$  were added to the flow.

A LaVision Flowmaster 3S PIV/PTV system was used to control the firing of the lasers and synchronize image capture with a digital imager, a 1280 x 1024 pixel cross-correlating camera with 12-bit resolution. The camera axis was perpendicular to the laser sheet and recorded the in-plane motion of the tracer particles. The light sheet was sufficiently thick to reduce the number of particles that entered or exited the light sheet due to strong cross-plane flow velocities. The camera was contained in a waterproof housing within the test section of the water tunnel. The image field-of-view was 127 x 101 mm for the  $r$  and  $x$  coordinates, respectively, and the lenses on the camera were chosen to have a depth-of-field much larger than the thickness of the light sheet. The PIV images were spatially calibrated by taking images of a registration target in the image plane. Images of the target were taken in the filled test section. The double-pulsed PIV images were analyzed using the La Vision software DaVis version 5.4.4. An adaptive multi-pass image process was employed starting with interrogation windows of 64 x 64 pixels and repeating with a final interrogation window of 32 x 32 pixels. The spatial resolution of the velocity vector field is 0.75 mm. Typically, the bad vectors were fewer than 10% before post processing. A three-by-three Gaussian smoothing filter was applied to the vector fields. Averages were calculated from 532 individual PIV images. With the advantage of the high spatial resolution of the PIV vector fields, assessment of the instantaneous axial and radial velocity in the plane of the laser sheet was possible.

PIV was used to take instantaneous “snap-shots” of the flow going through the propeller. The PIV data consisted of roughly 200 images of the flow field at each of eight different propeller angular positions covering a single blade passage. The PIV data can be used to quantify the magnitude of the flow variations through the propeller.

## Results

### Dynamometer

For reference and comparison, thrust and torque were measured in the ahead condition. The results for the thrust and torque coefficients,  $K_T$  and  $K_Q$ , respectively, are presented in Figure 6 for  $0.27 < J < 0.89$  at 650 rpm. The experiment was repeated 3 weeks later at 660 rpm. For reference, the straight lines in Figure 6 are linear regression fits to the repeat sensor 1 data,  $K_{T1}$  and  $K_{Q1}$ . The reproducibility of the data was quite good especially for  $K_{T1}$ . The largest differences occurred between thrust sensor 1 and 2,  $K_{T1}$  and  $K_{T2}$ . The results for  $K_{T2}$  were systematically higher, and they were reproducible. As the figure indicates, both thrust and torque decrease linearly over the range of  $J$ .

The results for crashback are presented in Figure 7, where the symbols are for the water tunnel data and the lines are from towing tank open water data. In this case for the tunnel data, the differences between the two sets of transducers are much smaller. The data were repeated 3 days later at  $J = -0.5$  and  $-0.7$  with very good results. The data scatter appears to be slightly higher than in the ahead case. The maximum for both thrust and torque occurs at  $J \sim -0.5$ . The maximum in unsteadiness also occurs at this value as discussed subsequently. PIV and LDV measurements were taken at  $J = -0.5$  for comparison.

In Figure 7, the discrepancy between the towing tank open water data and the water tunnel data is quite evident. The difference in the water tunnel data is probably due to tunnel boundary effects or the differences in the hub boundary conditions. The towing tank data lies below the water tunnel data, where the blue line (upper line) is for towing tank thrust coefficient,  $K_T$ , and the red line (lower line) is for the torque coefficient,  $K_Q$ . Unfortunately, this difference introduces uncertainty in the comparison of measurements to predictions, where tunnel effects are not included. However, the peak values occur at the same  $J$ .

The effects of Reynolds number on thrust and torque in crashback are shown in Figure 8 for  $J = -0.5$  and in Figure 9 for  $J = -0.7$ . Over the Reynolds number range of  $4$  to  $9 \times 10^5$ , the thrust coefficient appears to be constant while the torque coefficient appears to have a slight downward trend.

The variation in loads for crashback are presented as the standard deviation,  $\sigma$ , relative to the mean in Figure 10 and Figure 11 for thrust,  $T$ , and torque,  $Q$ , respectively. The data are plotted versus the absolute value of the advance ratio so that the ahead and crashback conditions can be more easily compared. As the figures indicate, the standard deviation in crash back is significantly higher and the data scatter larger than in the ahead condition. Most of the data were low pass filtered at 100 Hz and sampled at 1000 Hz, and the time interval was 5 s. The peak value in crashback occurred at  $J = -0.5$ . The data scatter was less for  $J > -0.4$  and  $J < -0.8$ . The lowest value in the standard deviation for crashback occurred at  $J = -1$ . For the same values of  $J$ , the standard deviations in thrust and torque were approximately the same; consequently, both thrust and torque exhibit the same data trends. At  $J = -0.5$ , the maximum values of thrust and torque were 0.25 and 0.23, respectively. The peak in the unsteady response curve of Figure 10 and Figure 11 corresponds to the maximum in the mean values of Figure 7.

A significant reduction occurred in data scatter for the data that were low pass filtered at 200 Hz and sampled at 2 kHz. However, the reduced scatter was the result of the longer

sampling interval. In this case, the sample interval was 30 s in comparison to 5 s for the other data. These results indicate that the sampling time should be greater than 30 s for improved statistical stability of the standard deviation for the crashback experiments.

In the ahead condition, the four data points near  $\sigma_T/T = 0.05$  for  $T1$  are apparent outliers and are not included in the plots. The cause may be the frequency setting in the low pass filter. Higher values did not occur in  $T2$  or repeat tests or in the torque.

As an evaluation of the quality of the signals, the signal to noise ratio,  $SNR$ , was computed for the data. The noise level was computed from the statistics from the transducers during spin down of the propeller to zero at no flow. The maximum rotational rate in the time series for the statistics was 14.5 rpm. The  $SNR$  in dB was computed from the following formula

$$SNR = 20 \log(\sigma_x / \sigma_N) \quad (4)$$

where  $\sigma_N$  is the standard deviation of the instrument noise. The results are shown in Figure 12 and Figure 13, for thrust and torque, respectively. The data trends are similar to those described previously. The data indicates that the signal quality is reasonable and that the information in the standard deviation is meaningful.

For the maximum unsteadiness in torque in crashback at  $J = -0.5$ , the  $SNR$  is about 32 dB. This value corresponds to the  $SNR$  of a tape recorder [5]. As another comparison, a 5-bit digitizer has a  $SNR$  of 30 dB while a 12-bit digitizer has an  $SNR$  of 80 dB [5]. For torque at  $J = -0.5$ , the  $SNR$  is 20 dB or the signal is 10 times the noise.  $SNR$  for the ahead condition is not particularly meaningful since the signal is about the same as the noise. For the thrust in ahead condition, the  $SNR$  was about 12 and constant with  $J$ . For torque, the signal was about the same as the noise and was not included in Figure 13.

The standard deviation of thrust and torque are presented as a function of Reynolds in Figure 14 and Figure 15, respectively. The data scatter is too large for any conclusions about Reynolds number effects, but the torque seems to indicate a downward trend with Reynolds numbers. Longer time averages are necessary for statistical stability. In general, the results from the standard deviations of the loads are good indicators of the highly unstable flow in crashback.

## Flow Visualization and Cavitation

Some of the essential flow features were visualized with laser light sheet illumination and strobe light illumination. Both methods indicated highly unsteady flow in crashback. Results for crashback presented here are only for  $J = -0.5$  at  $-700$  rpm, tunnel speed of 1.778 m/s (5.83 ft/s) and tunnel pressure of 110 kPa (16 psia). In Figure 16, the cross section of the vortex ring is shown at a single instant of time; however, this flow feature is highly random. This particular frame was selected because it is quite similar to the results measured by LDV with long time averages, which will be described in the next section.

Cavitation in the ahead condition is presented in the two photos of Figure 17 and Figure 18. In this case, the flow is quite steady. The figures indicate the tip vortices from each blade and a hub vortex.

In contrast, a sequence of photographs of cavitation in crashback is presented in Figure 19, where the frame rate was 29.97 per second. The strobe rate was not quite uniform, but typically the propeller was strobed every fifth frame for a  $\Delta\tau = 0.167$  seconds. Cavitation is highly

random. Large areas of cavitation occur at the blade leading edge on the downstream side, which is normally the trailing edge in the ahead condition. This flow feature is shown at various blades in Figures 18 (a), (e), (f), and (g), while cavitation on the blades is significantly less in Figures 18 (b), (c), (d), and (h). These large areas of cavitation tend to form near the hub and move outward toward the tip. The cavitation bubbles are, then, dissipated by the unsteady recirculation region around the propeller.

## Laser Doppler Velocimetry

The spanwise loading can be represented from the measured circumferential average tangential velocity using LDV measured at  $x = 0.23$ . Comparison with computations is shown in Figure 20. The circulation  $G(r)$  is defined as,

$$G(r) = rU_t(r) / N_b \quad (5)$$

where  $N_b$  is the blade number.

Wake contraction is apparent, and the very large effect of the tip vortex can be seen. From the hub to the 0.8 radius, the measured result is consistent with the over prediction of thrust and torque (Table 5). The potential influence of the local tip loading on the overall thrust and torque prediction is clear from the circulation.

Figure 21 shows the streamwise blade wake of propeller 4381 at  $J = +0.3$  in the rotating frame of reference. The blade flow appears attached but shows a significantly thicker blade wake than typically is observed for propellers operating at design  $J$ . Also seen is the intense tip vortex. The hub flow has not sufficiently developed at  $x = 0.23$  for the occurrence of a large hub vortex. The blade wake at 0.7R is shown in detail in Figure 22. The high gradient side of the wake is convected from the pressure side of the blade, while the lesser gradient side is from the suction side of the blade where the pressure distribution is adverse due to the high blade angles of attack. The turbulent kinetic energy is consistent with foil wakes at high angles of attack and does not indicate separated flow.

Section drag coefficients were tabulated as twice the momentum thickness in the wake and compared to those of Jessup [6] for Propeller 4119 operating at design  $J$ , shown in Figure 23. Significant increase in blade drag is seen as compared to sections at ideal angle of attack. The increase in section drag was used to recompute the open water performance at  $J = +0.3$  as presented in Table 5. The computed  $K_T$  moves toward both the tow tank and water tunnel results, but  $K_Q$  increased well beyond the test results. The efficiency prediction is improved using the measured section drag. Differences in the predicted and measured spanwise circulation distribution in the tip region appear to be as significant as the refinement of the blade section drag.

Additional results of the LDV measurements are presented in a series of contour plots. Since the flow in crashback is highly unsteady, emphasis is placed on the total kinetic energy (TKE), which is defined as follows:

$$TKE = q^2 / 2 = (\sigma_{Ur}^2 + \sigma_{Ut}^2 + \sigma_{Ux}^2) / 2 \quad (6)$$

The initial plots indicate the inflow to the blades and the wake flow. The contours are normal to the streamwise velocity vector,  $V_s$ , defined in Eqs. (2), which is essentially the flow relative to

the blade. In this format, structure of the tip vortex in the ahead condition is shown in cross-section.

The contour plots in the ahead condition at  $J = +0.3$  are shown in Figure 24 for the inflow and wake flow. The total kinetic energy is normalized with the relative freestream flow,  $V_\infty$ , defined in Eq. (1). For the inflow, the turbulence is relatively low. Near the tip, the level is about the background noise level of 1.5 % for the LDV. The blade wake and tip vortex are clearly shown in Figure 24 (b). From inspection of the wake, no flow separation occurs on the blade. A higher resolution plot of the tip vortex with streamlines is shown in Figure 25.

The results for crashback are quite different as indicated in Figure 26 and Figure 27 for  $J = -0.5$  and  $-0.7$ , respectively. The upstream and downstream contours are very similar, and the total kinetic energy is quite high in comparison to the ahead case. For  $J = -0.5$ , the level is over 0.6 at the hub and about 0.2 at the tip for both upstream and downstream. The levels are lower for  $J = -0.7$ . These high values are indicative of highly unsteady flow rather than turbulence. For a direct comparison, the color scales for these two figures are the same. As these figures indicate, no coherent flow structures occur relative to the blade similar to the wake flow and tip vortex flow of Figure 24 (b) and Figure 25. However, coherent structures of from the blade wake are more apparent in the contour plots of the streamwise velocity component in Figure 28.

The three-dimensional flow structure for crashback is indicated by contour plots in the  $x$ - $r$  plane in Figure 29 through Figure 32. For  $J = -0.5$ , the three velocity components are presented in Figure 29. The dominant features of this figure are the large recirculation zone and the ring vortex near the propeller tip. These features are similar to the light-sheet flow visualization of Figure 16. Another significant characteristic of the ring is the slightly negative tangential velocity component ( $U_t \sim -0.1$ ) in the direction of the propeller rotation. Also, a high-speed tangential velocity component ( $U_t \sim -0.8$ ) is located on the upstream edge of the propeller in the direction of the propeller rotation.

The contour plot of the total kinetic energy in Figure 30 is significantly different from the velocity contour plot. For a turbulent shear flow, the organized structures shown in a contour plot for velocity are similar in shape to that of kinetic energy. The shapes are similar because regions of high velocity shear are also regions of high turbulence. The contour plot of the streamwise velocity for the ahead condition in Figure 21 is similar to that of the kinetic energy in Figure 24 (b). For crashback, most of the kinetic energy is from the unsteadiness of the flow. Consequently, similarities between velocity and kinetic energy do not seem to exist from a comparison of Figure 26 and Figure 28.

In Figure 30, most of the recirculation zone has a kinetic energy the same order of magnitude ( $q = 1$ ) as the tunnel velocity. The large magnitude is due to the unsteadiness in the flow at long time scales rather than traditional turbulence at the smaller scales. For example from Townsend [7], values of maximum  $q$  for turbulent shear flows are 0.49, 0.39, and 0.28 for the wake, jet, and boundary layer, respectively. In comparison, the highest value this propeller is located near the blade tip where  $q \sim 1.5$ . The character of the flow for  $J = -0.7$  in Figure 31 for mean velocity and Figure 32 for  $q$  is very similar to  $J = -0.5$ ; however, the levels are lower. The core of vortex ring is closer to the blade tip for  $J = -0.5$ . The ring is further from the centerline and further downstream for  $J = -0.7$ .

## Particle Imaging Velocimetry

A very large data set of PIV images has been acquired. Only a limited number of data sets are presented to provide an indication of the data available. Movies must be viewed for a full appreciation of the data. The measurements are high resolution in the immediate area of the propeller blade. Only the mean velocities and instantaneous velocities are presented in the following results. The purpose was to provide detailed information on the flow physics near the propeller blade. The development of the tip vortex is shown for  $J = +0.3$  at the blade tip shown in Figure 33. Relative mean velocity vectors are presented for emphasis of the flow around the vortex core. This figure is an average of 120 image pairs. This figure is not significantly different than the contour plot of the velocity vectors for a single measurement. The vortex at the blade tip is highly stable.

For comparison, the tip vortex for the LDV measurements is shown in Figure 24 (b). In this case, the blade wake is measured downstream of the blade at  $x/r = 0.23$  while the PIV measurements of the vortex were near the blade tip. Although a direct comparison is not possible, both sets of data demonstrate that the tip vortex at  $J = +0.3$  is highly stable.

In the subsequent figures, the results are presented for crashback for  $J = -0.5$  and  $-0.7$ . As described previously, the flow in crashback is very unsteady. In Figure 34 through Figure 37, the results for the mean axial and mean radial velocity components for PIV are compared to LDV. For  $J = -0.5$ , the PIV data are an average of 998 image pairs while for  $J = -0.7$  the averages are for 1068 image pairs. In general, the contour plots for LDV and PIV are qualitatively similar. Some of the differences in the details are from the finer spatial resolution of the PIV. Only half of the PIV vectors are shown in the figures of the averages for clarity. For direct comparison, the data for PIV and LDV are plotted with the same scales. The LDV data are a smaller section of the same data presented in Figure 29 through Figure 32.

In Figure 34 for the radial component of velocity at  $J = -0.5$ , details of highly organized flow structures are evident immediately upstream and downstream of the blade are evident in the PIV data but not the LDV data. These differences may be due to the higher spatial resolution of the PIV measurements. For the axial velocity, highly organized structures also appear in Figure 35 (a) for the PIV data. One significant difference is an airfoil shaped region near the downstream edge of the blade toward the hub for the PIV data. The minimum magnitude of the velocity for the PIV data is significantly lower than LDV data by about half. Most of this region is red for the PIV data but blue for the LDV data. The source of this difference is unknown.

Similar organized structures occur at  $J = -0.7$  in Figure 36 and Figure 37. Again an airfoil shaped region occurs near the downstream edge of blade toward the hub in the axial velocity component in Figure 36 (a) for the PIV data. The magnitude of the velocity in this region is significantly lower for the PIV data.

Both the PIV and LDV data indicate significantly different flow characteristics near the blade between  $J = -0.5$  and  $-0.7$ . For the reverse flow near the tip on the downstream side of the blade a small radial component in velocity occurs at  $J = -0.5$  while the flow at  $J = -0.7$  tends to be parallel to the axis of the propeller. Upstream of the blade tip the outward radial flow is much stronger for  $J = -0.7$ .

Additional details for  $J = -0.7$  from a mosaic of 6 PIV images is presented in Figure 38 for the streamline velocity. The mosaic shows details of the flow outside the propeller tip region.

The upstream edge of the recirculation zone may be seen in this figure. The streamlines are similar to those of Figure 31 and Figure 37.

An example set of instantaneous velocity vectors from a single image pair is shown in Figure 39 and Figure 40 for  $J = -0.5$  and  $-0.7$ , respectively. Since the flow is highly unsteady, these figures should not be considered representative. However, they do indicate that the instantaneous results are significantly different from the average results presented in the previous figures of the average flow. The color scales in the contour plots of instantaneous velocity are different from the plots of the averages due to the broader range of data.

One of the more interesting features of the instantaneous PIV data is the vortical structure at the blade tip shown in Figure 39. This vortex is similar to the one in for  $J = +0.3$ , but it is highly random and sheds from the blade tip as indicated in the movies of the PIV data. This feature is probably the cause of the high values of  $q$  near the blade tip shown in the LDV measurements of Figure 30 and Figure 32. A similar feature although not as strong occurs in Figure 40. The flow on the upstream side of the blade has trends similar to those of the average plots. For  $J = -0.5$ , the flow is in the axial direction while at  $J = -0.7$  the flow has a strong outward radial component. On the upstream side the instantaneous flow is quite different from the average flow. For  $J = -0.5$  downstream of the blade tip, the flow on average is in reverse while the instantaneous flow in Figure 39 is in the direction of the tunnel velocity with an inward radial component. In Figure 40, the instantaneous flow is inward radially while the average is reverse flow in the axial direction. Although the instantaneous plots of Figure 39 and Figure 40 are not necessarily representative, they do indicate a significant difference from the mean flow. They also represent the highly unsteady nature of the flow.

A hypothesis was developed from observation of the individual PIV images. The ring vortex appeared to descend from its time average location around 1.7 fraction of tip radius to locations inside of the tip radius. When this occurred, the axial velocity in the tip region reversed direction from its time average sense. This would produce a large increase in the angle of attack of the blade sections near the tip, and cause a large increase in tip loading. The tests of Jiang [8] described the convection of the ring vortex downstream and its periodic breakup. This global behavior could have resulted in transient movement of the vortex inboard of the blade tip resulting in the extreme reversed tip flow, that is believed to cause excessive blade tip loading.

The multiple PIV records were ordered by the occurrence of the reversed flow at the tip. From 1000 PIV records, the images were ordered from “most extreme” where reversed tip flow occurred to “best” where the tip flow was similar to the time average flow. Three samples of the “most extreme”, “8th extreme”, and “best” propeller flow is shown in Figure 41. Figure 42 shows the most extreme axial velocity profiles and a computed average. Figure 43 compares the extreme profile to the time average.

## Conclusions

Quantitative and qualitative results have been presented on propeller 4381 in crashback and compared to results in the ahead condition. In crashback, the flow is highly unsteady in comparison to the ahead condition, and results from cavitation, laser light sheet flow visualization, propulsion, and detailed flow measurements by LDV and PIV characterized the unsteadiness. Qualitatively, the results are in agreement with an unsteady vortex ring predicted with CFD by Davoudzadeh, et al. [3]. In ahead at  $J = +0.3$ , propeller 4381 has a typical tip

vortex as indicated by LDV and PIV measurements and cavitation and has a hub vortex as indicated by cavitation. The following is a summary of the key features in crashback:

- **Vortex Ring.** Laser light sheet flow visualization and LDV measurements indicate a large recirculation region with reverse flow at the propeller. A trapped vortex ring occurs near the propeller tip for both  $J = -0.5$  and  $-0.7$ . At  $J = -0.7$ , the core of the ring is located further downstream and outward radially in comparison to  $J = -0.5$ . On average, the ring rotates at a slow speed in the direction of propeller rotation. The highest tangential flow occurs at the leading edge of the propeller.
- **Unsteady Flow.** The flow is highly unsteady. The circulation region has a high value of total kinetic energy as measured by LDV with a value of the same order of magnitude as the tunnel velocity ( $q \sim 1$ ) for  $J = -0.5$ . The maximum occurs near the blade tip. At the same time, torque and thrust have very high standard deviations. In general, the standard deviation as measured by LDV and torque and thrust sensors are higher for  $J = -0.5$ . The peak values in the standard deviation for both torque and thrust occur at  $J = -0.5$  for measurements over the range of  $-1 < J < -0.2$ . The high values in the standard deviation of thrust and torque appear to correlate with the high values of  $q$  at the blade tip as measured by LDV. The results for LDV and propulsion are compared in Table 6.
- **Cavitation.** Propeller cavitation is also highly unsteady and random. Cavitation occurs on the downstream side of the blade at the leading edge, which is the trailing edge for ahead. Cavitation occurs randomly along the edge of the blade. During a single time interval, some blades cavitate, while some do not. After the cavitation bubbles leave the blade, they are dissipated by the unsteady recirculating flow of the propeller.
- **Reynolds Number.** In crashback,  $K_T$  is constant over the Reynolds number range of 4 to  $9 \times 10^5$ , while  $K_Q$  has a slight downward trend with increasing Reynolds number. The data scatter in the standard deviation is so large that a definitive conclusion about a Reynolds number effect is not possible; however, the standard deviation in  $K_Q$  may have a downward trend with increasing Reynolds number. Longer time averages are necessary for a reduction in data scatter.

Since the flow is highly unsteady and random, long time averages are necessary for the second order statistics (standard deviation). Long time averages are necessary for the propulsion, LDV, and PIV data for stable statistics. For the LDV measurements, each point was a 90 second average. For the PIV data, averages of about 1000 image pairs were necessary. Much of the propulsion data was acquired with 5-second averages. As a consequence, large data scatter occurred in repeat measurements of the standard deviation in the propulsion data. Data scatter was reduced significantly with 30-second averages. In future crashback experiments, the averaging should be evaluated and should probably be at least 60 to 90 seconds. From accurate estimates of the standard deviation, more accurate estimates of the extreme values are possible. The extreme value at the 95 % confidence level relative to the mean is then  $2\sigma_x$ .

The movies from the PIV data provide a quantitative measure of the unsteady character of the flow and may provide additional insight into the fundamental mechanisms on blade loading. In particular, the second order statistics (standard deviation) for the velocity components should be computed. This information may lead to a more detailed description of the localized loading.

The LDV data have already shown that high  $q$  values occur at the blade tip for  $J = -0.5$ . The PIV data may provide a better resolution of this observation.

The standard deviation for the thrust data also has a relatively high signal to noise ratio with values between 23 and 33 dB. The torque was lower with a peak SNR of 22 dB. These relatively high values indicate that significant information is contained in these signals. The averaged power spectrum from at least 50 individual time series should be computed to determine if signal is broadband or if relevant frequency information is available, which correlate with other measurement methods such as LDV or PIV. The current data set consists of a record length of 60,000 samples at 2 kHz over a 30 second time interval. This set can be sub-divided into records with lengths of 1024 samples for computation of spectra via FFT (Fast Fourier Transform). An average spectrum from 58 records could be computed with a frequency resolution of 2 Hz.

In addition to the previous comments, the following are recommended in future experiments for a better understanding of the flow physics in crashback. A laser light sheet should be located normal to the propeller blades to determine the character of flow separation. Strain gages should be installed on the propeller blades to correlate blade loading with the fluid flow. Finally, reduction in the operating time of a ship or submarine near  $J = -0.5$  for this propeller would reduce vibration and possibly extend propeller life.

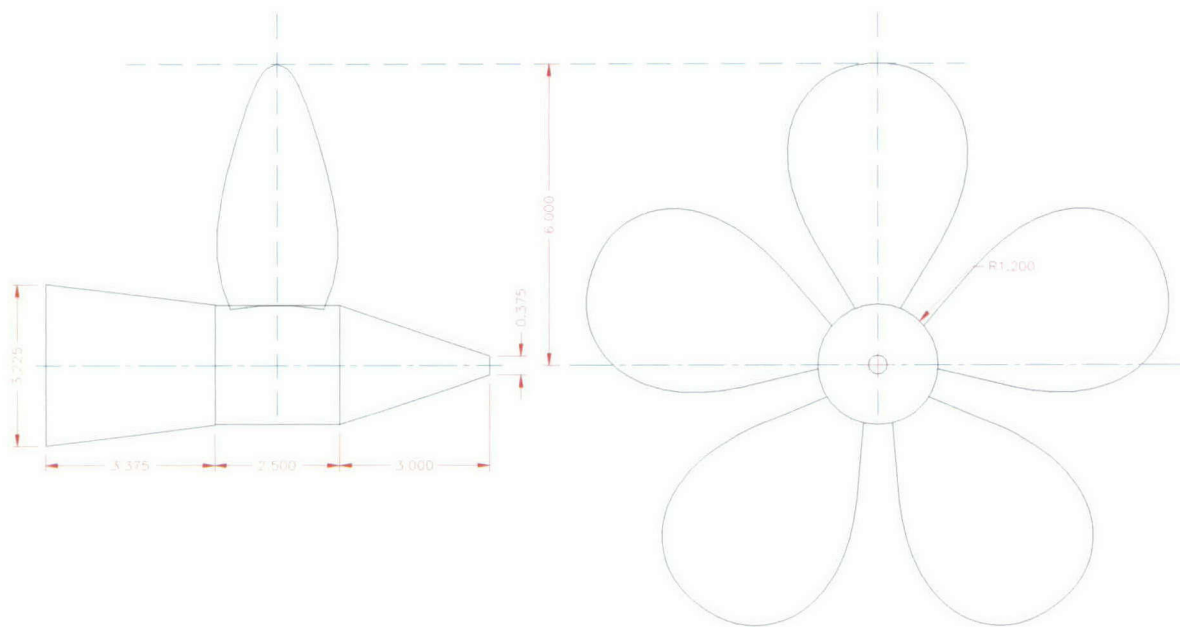


**Figure 1. Propeller 4381 Geometry**

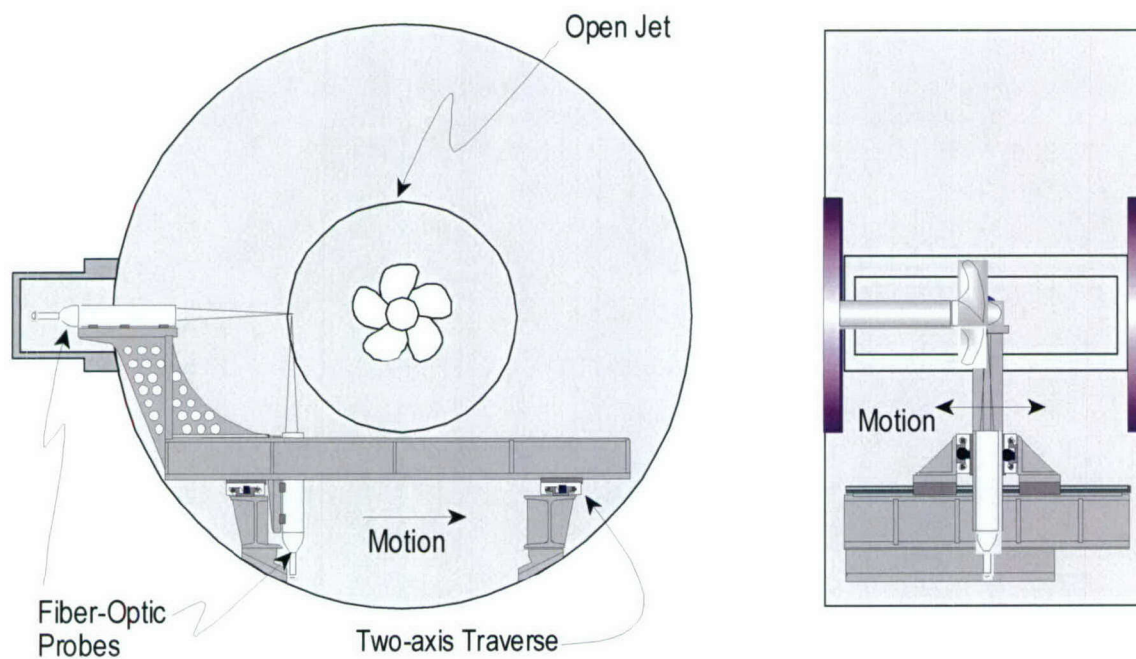


**Figure 2. Fiber-Optic Probes in the 36-inch Water Tunnel**

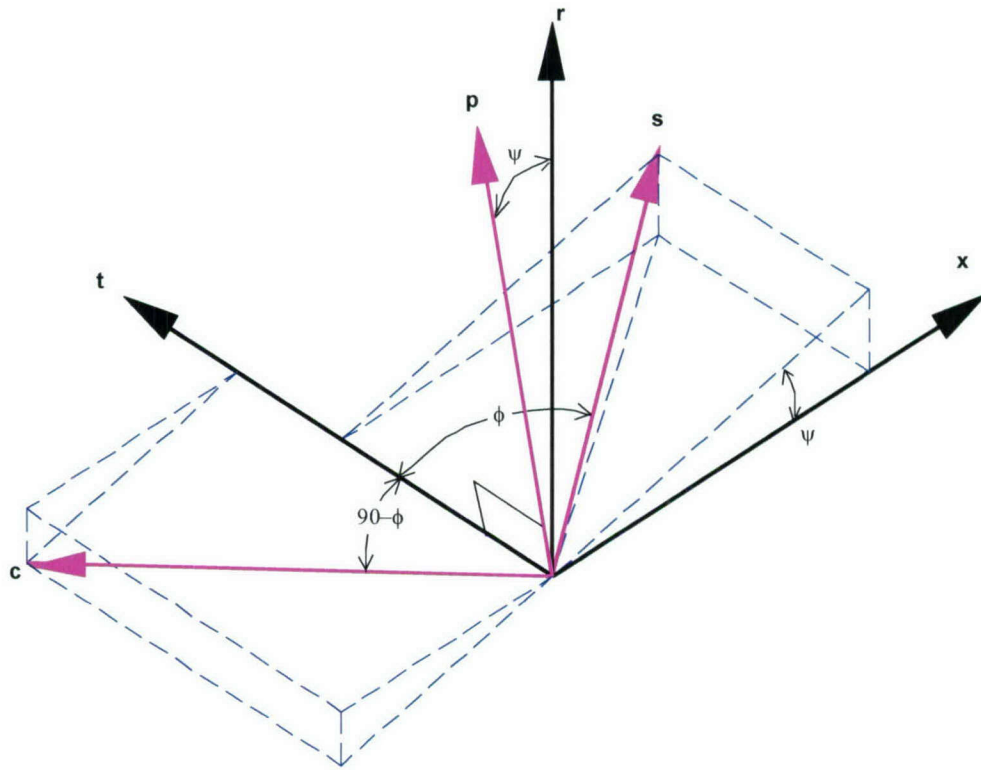


**Figure 3. Primary-Secondary Flow Coordinate System for LDV Measurements**

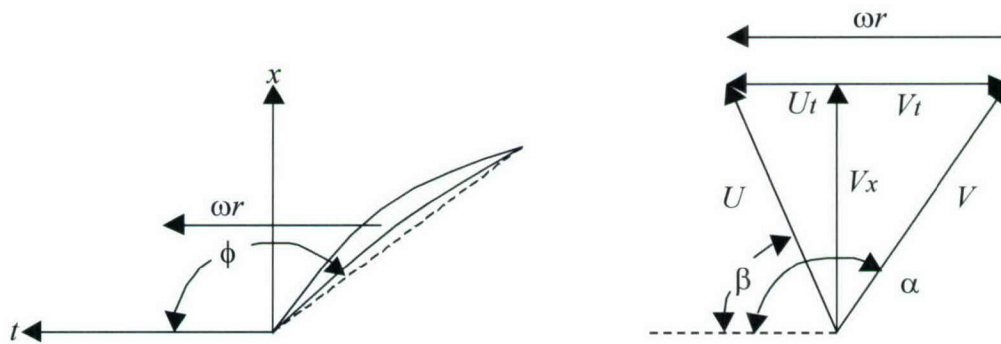


**Figure 4. Flow Vectors and Angles for LDV Measurements**

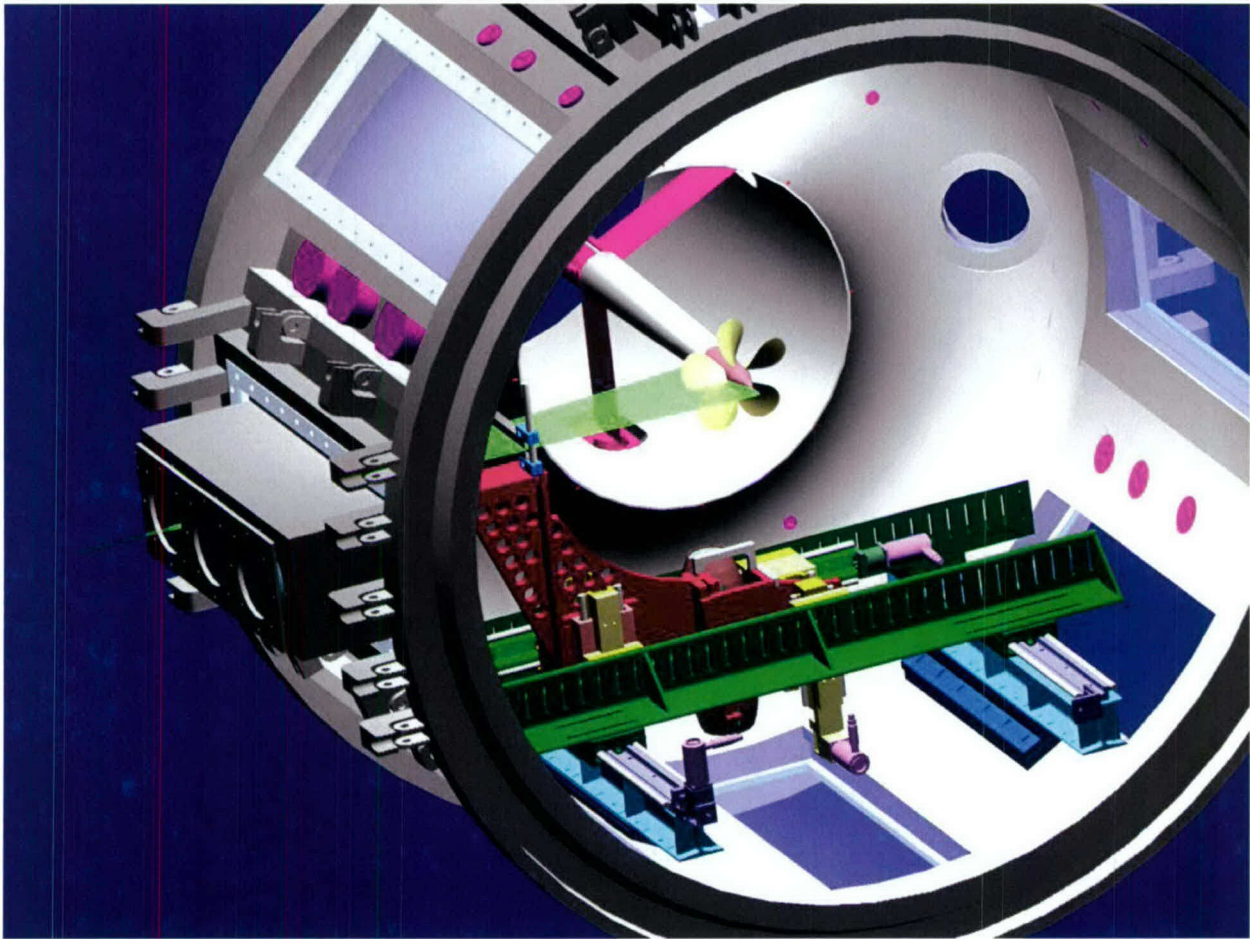


**Figure 5. PIV Experimental Arrangement in 36-inch Water Tunnel**

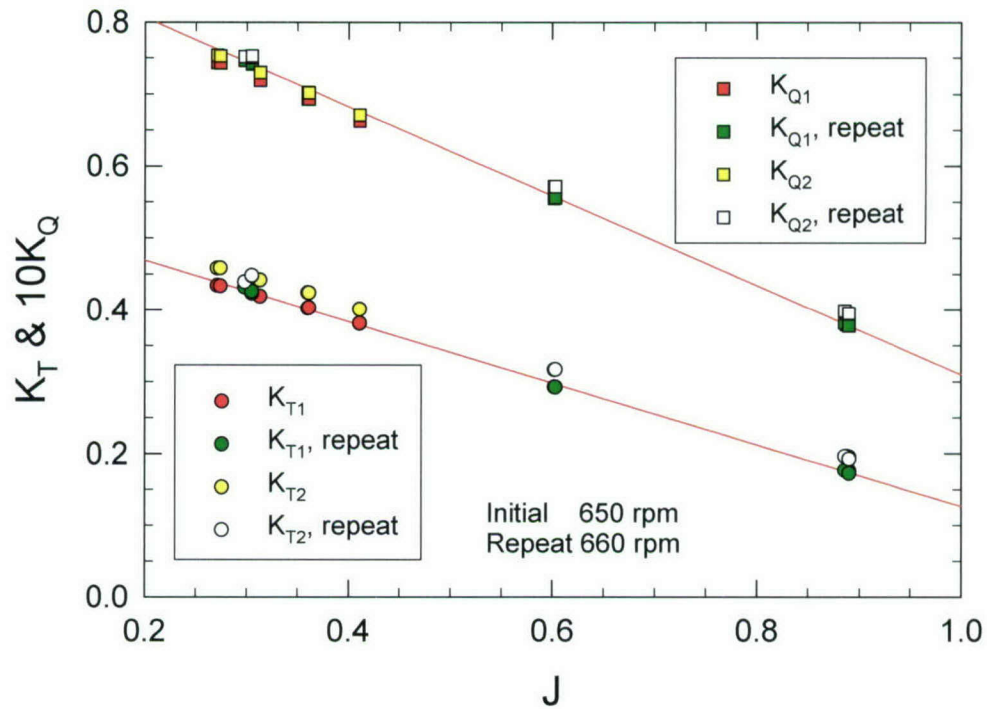


Figure 6. Thrust and Torque Coefficients for Ahead Condition at 650 and 660 rpm

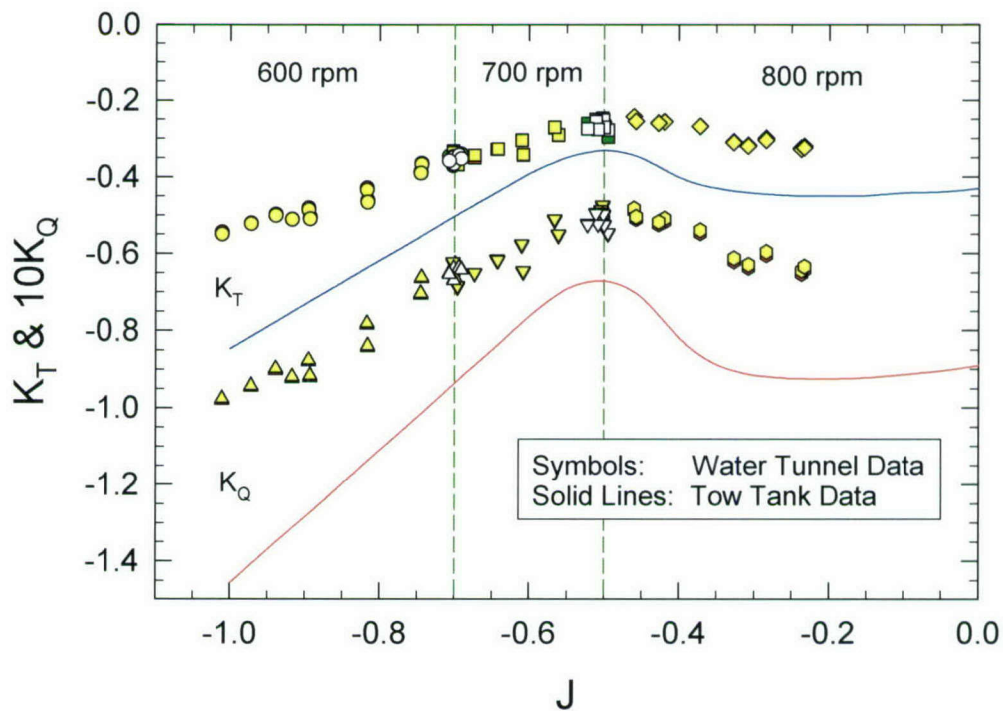


Figure 7. Thrust and Torque Coefficients for Crashback

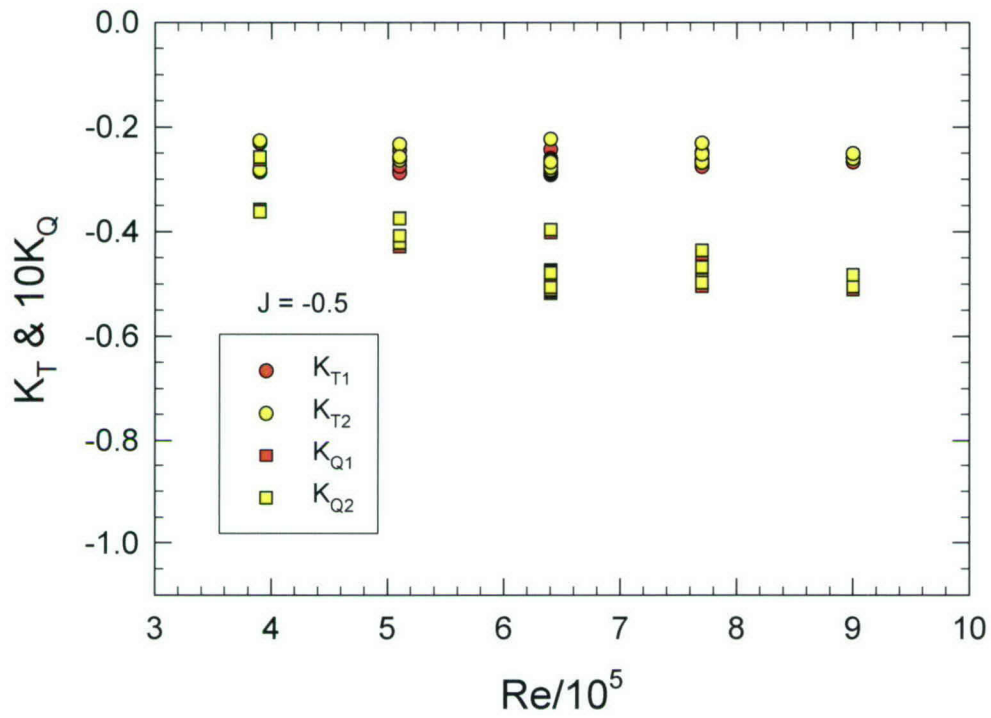


Figure 8. Reynolds Number Effect on Crashback for Thrust & Torque at  $J = -0.5$

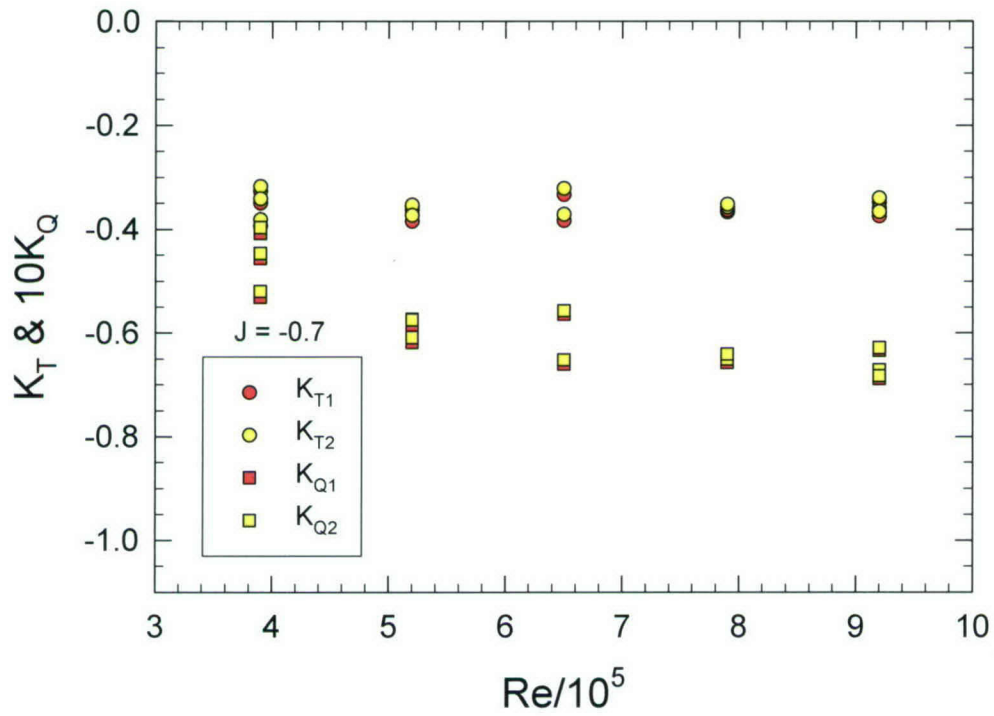
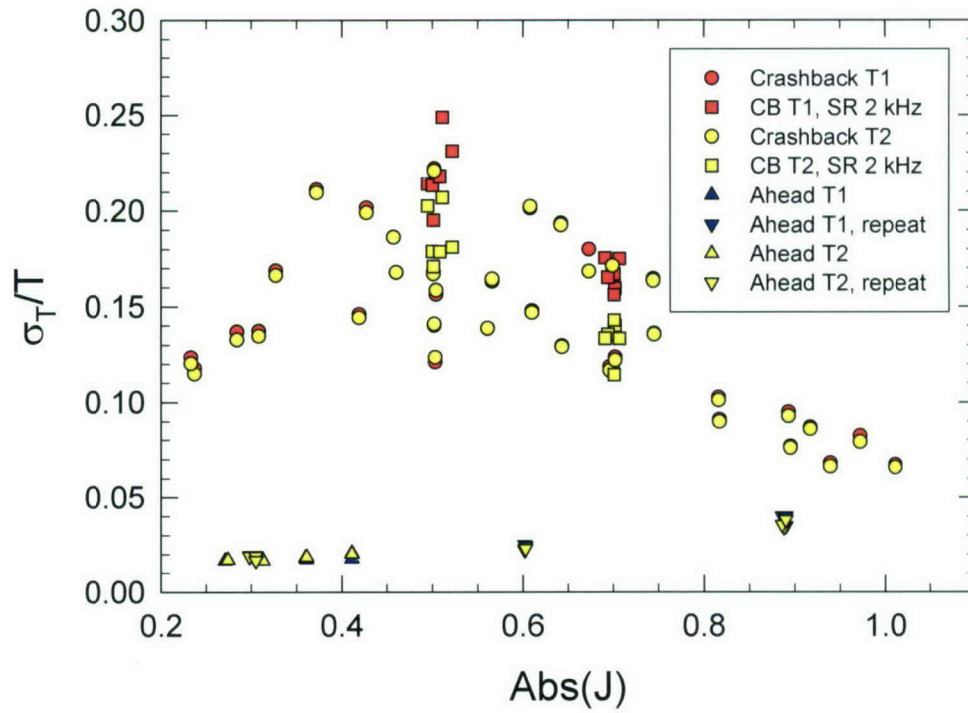
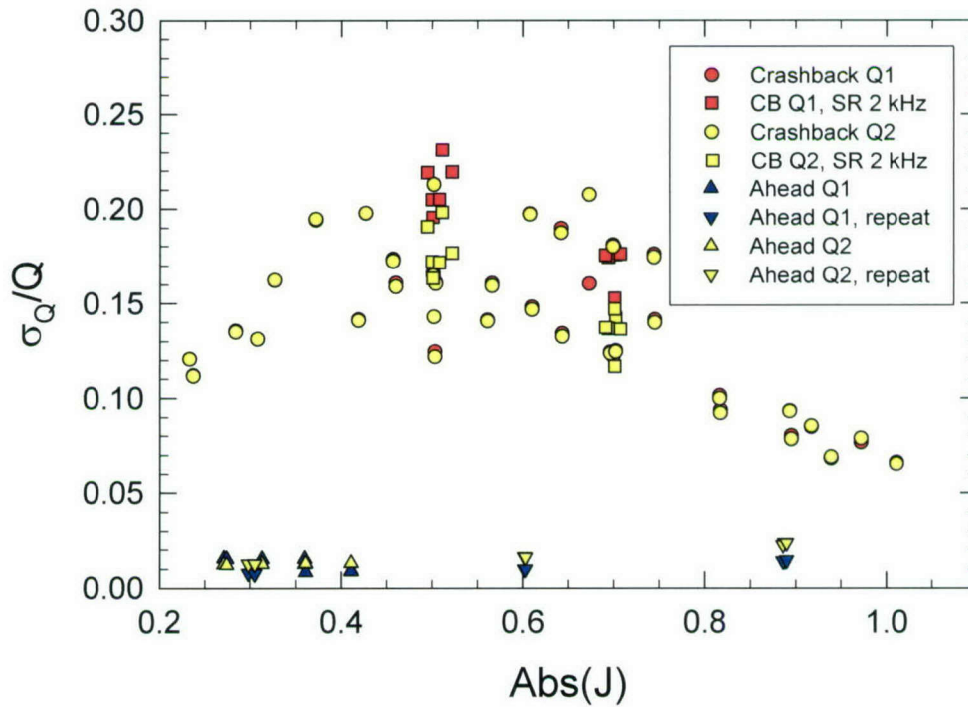


Figure 9. Reynolds Number Effect on Crashback for Thrust & Torque at  $J = -0.7$



**Figure 10. Standard Deviation of Thrust in Ahead and Crashback**



**Figure 11. Standard Deviation of Torque in Ahead and Crashback**

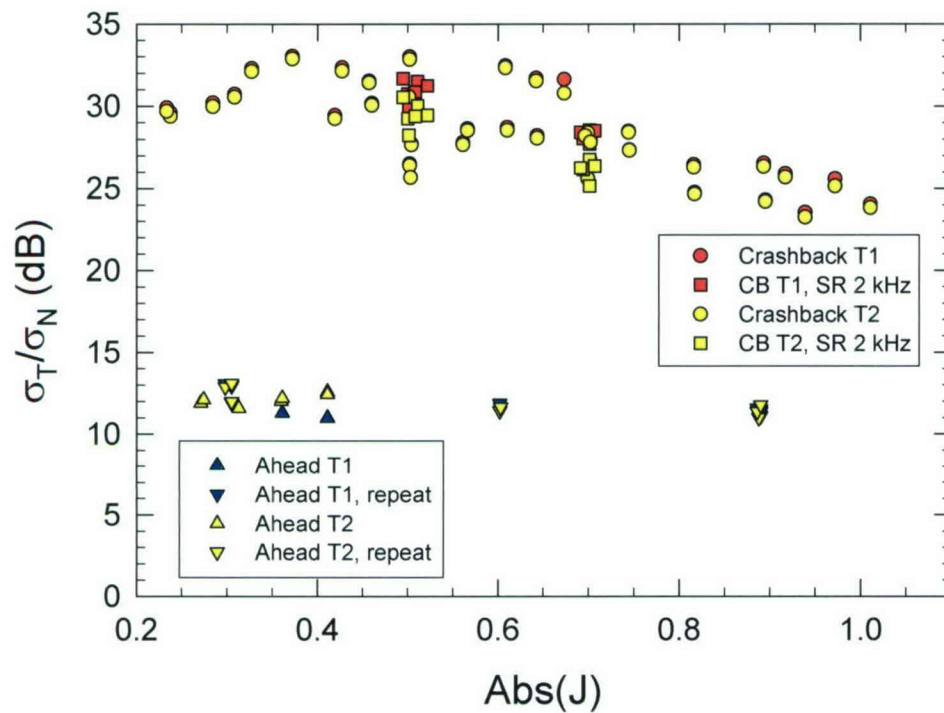


Figure 12. Signal to Noise Ratio for Thrust

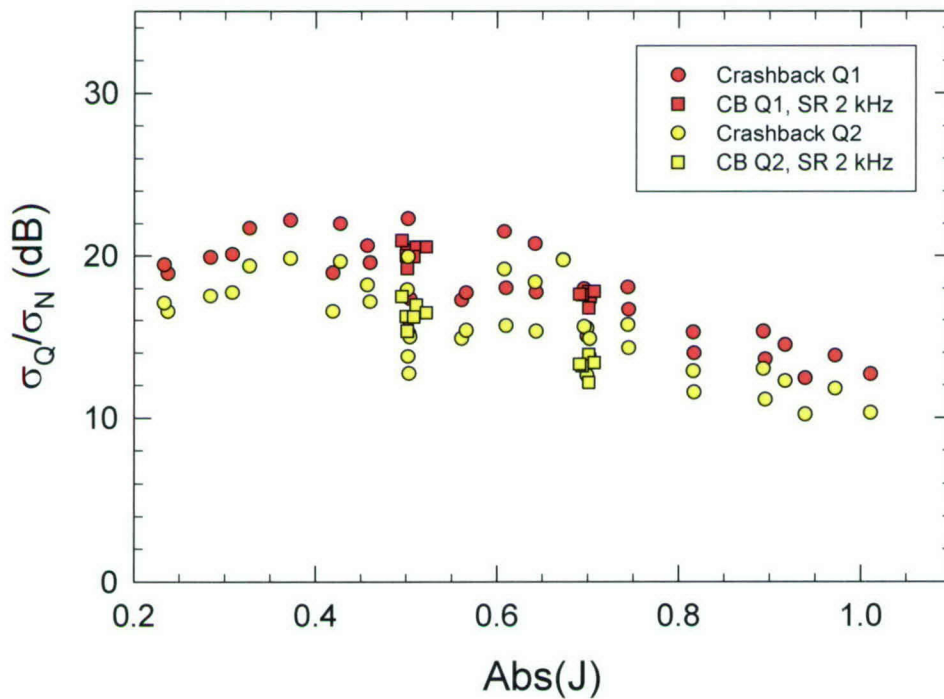


Figure 13. Signal to Noise Ratio for Torque

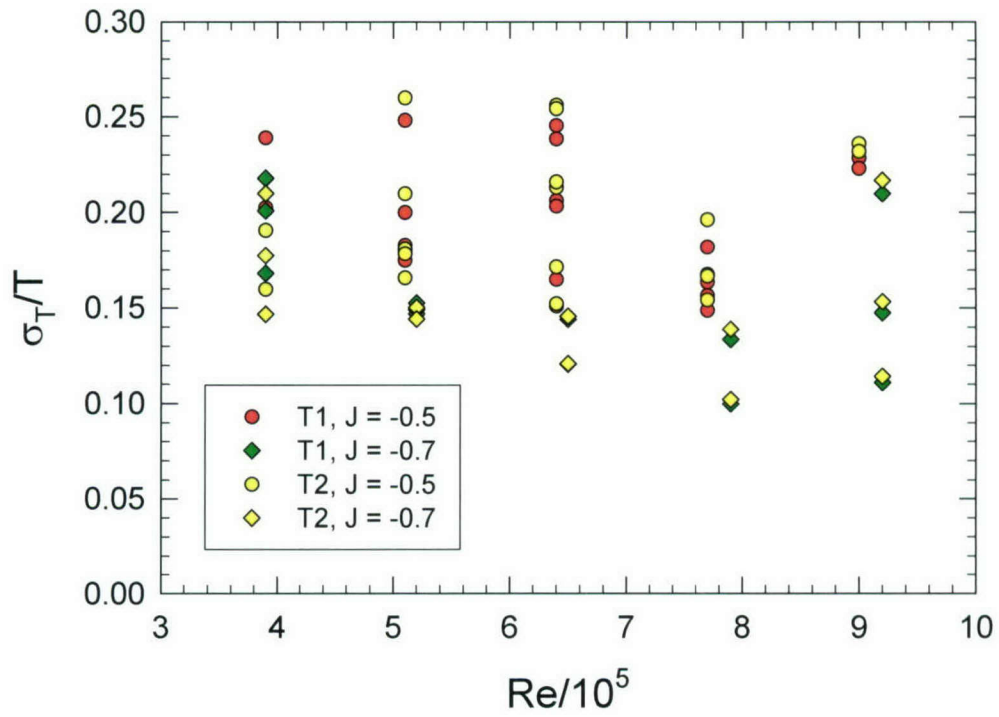


Figure 14. Reynolds Number Effect on Standard Deviation of Thrust

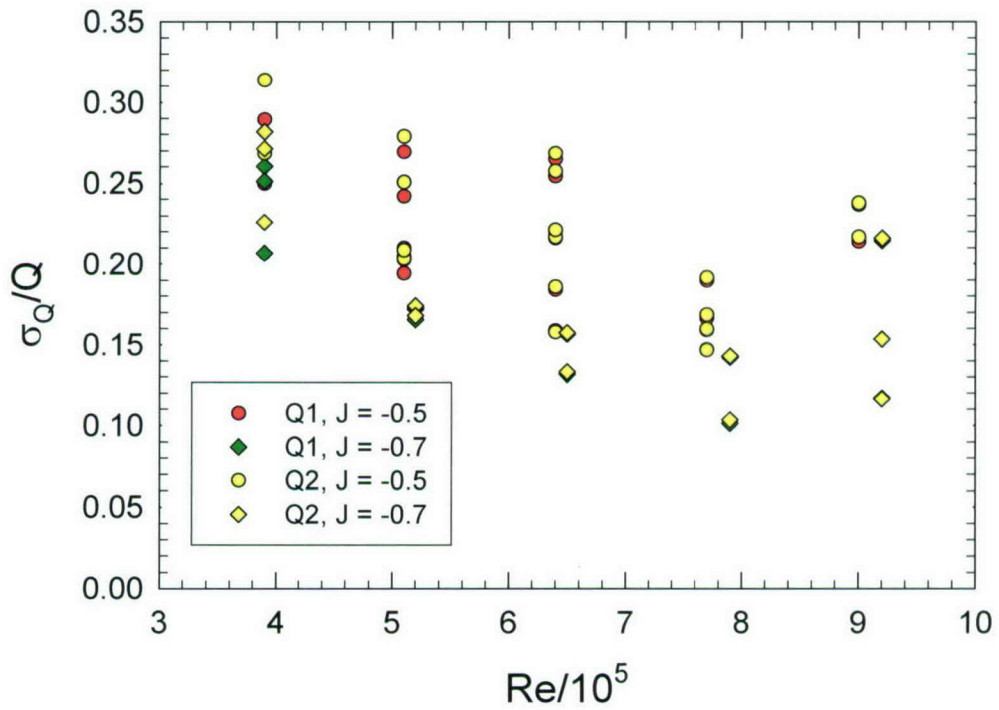
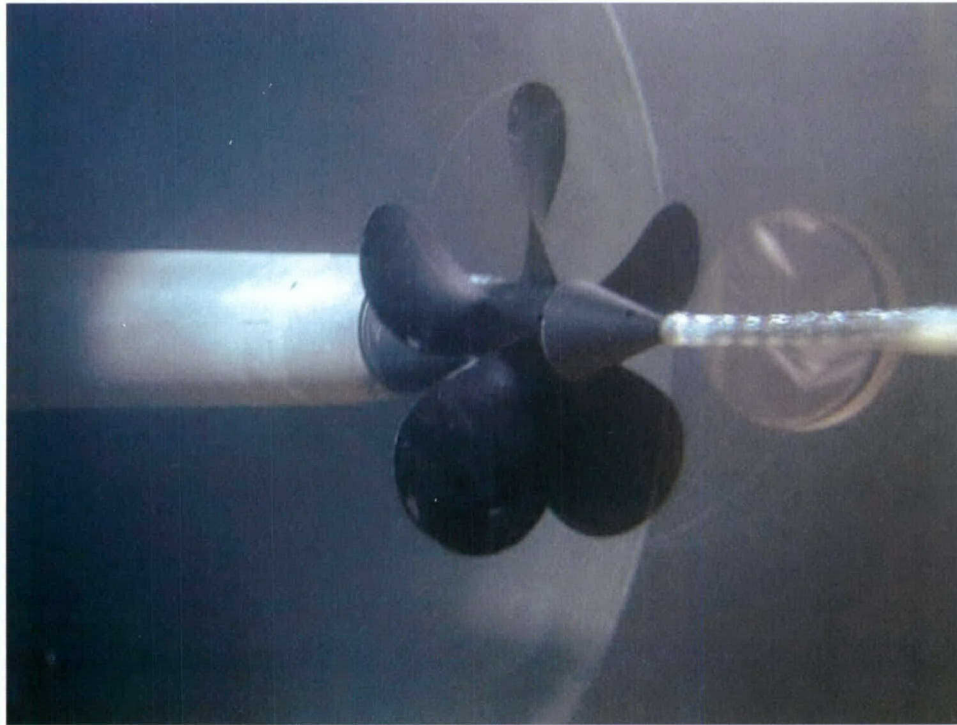


Figure 15. Reynolds Number Effect on Standard Deviation of Torque



**Figure 16. Laser Light Sheet Illumination of Vortex Ring for Propeller 4381**



**Figure 17. Hub Vortex Cavitation of Propeller 4381 in Ahead Condition**

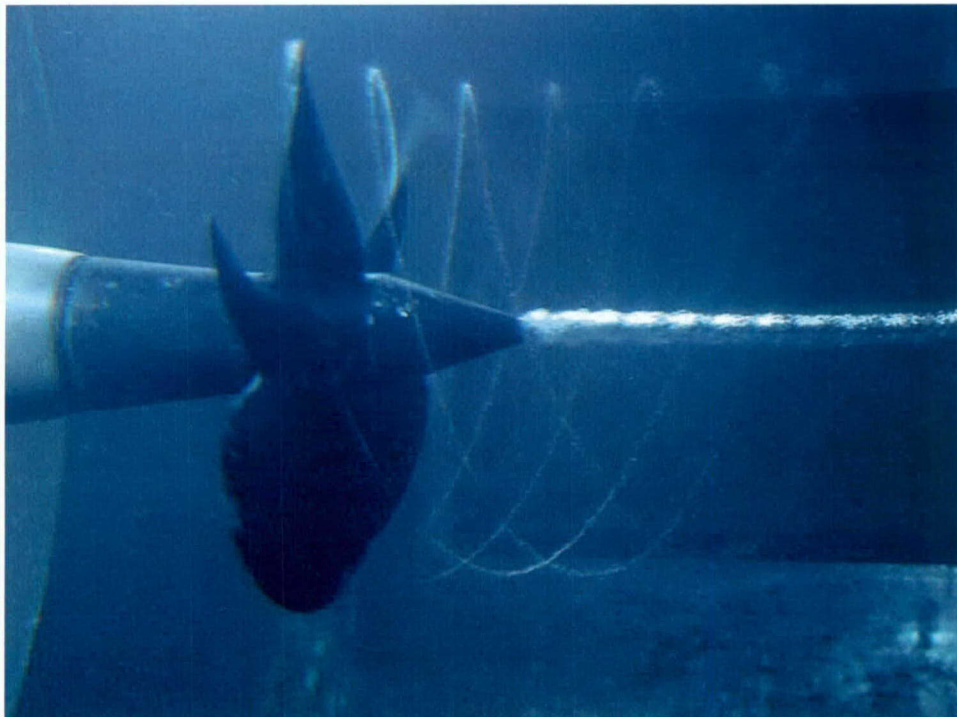
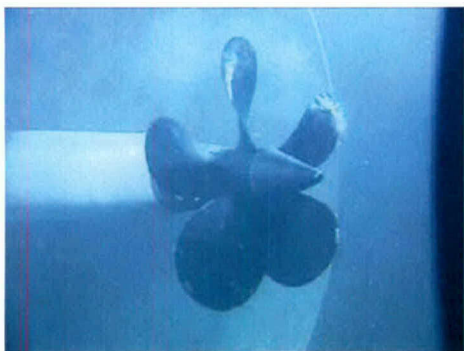
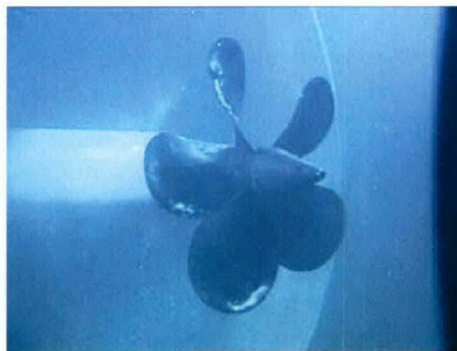


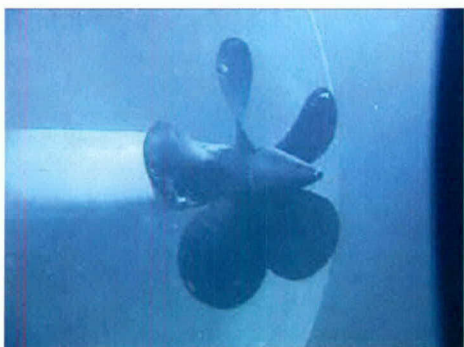
**Figure 18. Tip and Hub Cavitation for Propeller 4381 in Ahead Condition**



(a)  $\tau = 0.000$  s



(e)  $\tau = 0.601$  s



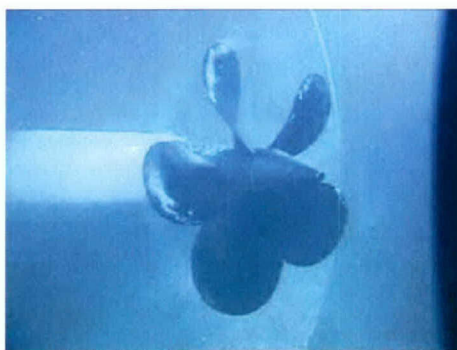
(b)  $\tau = 0.167$  s



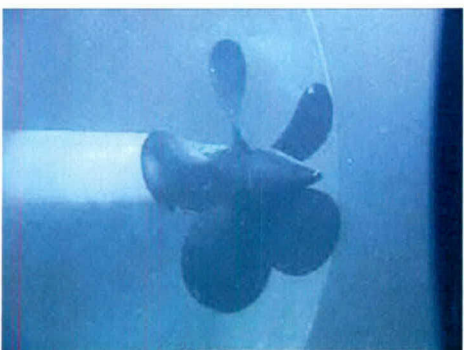
(f)  $\tau = 0.767$  s



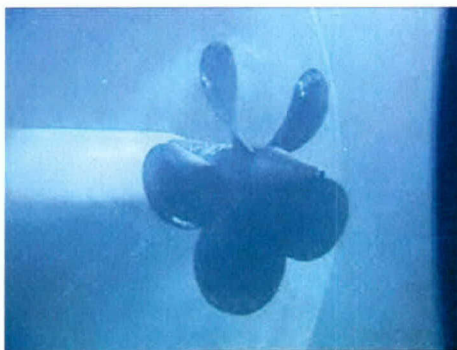
(c)  $\tau = 0.267$  s



(g)  $\tau = 0.868$  s



(d)  $\tau = 0.438$  s



(h)  $\tau = 1.034$  s

**Figure 19. Cavitation of Propeller 4381 in Crashback**

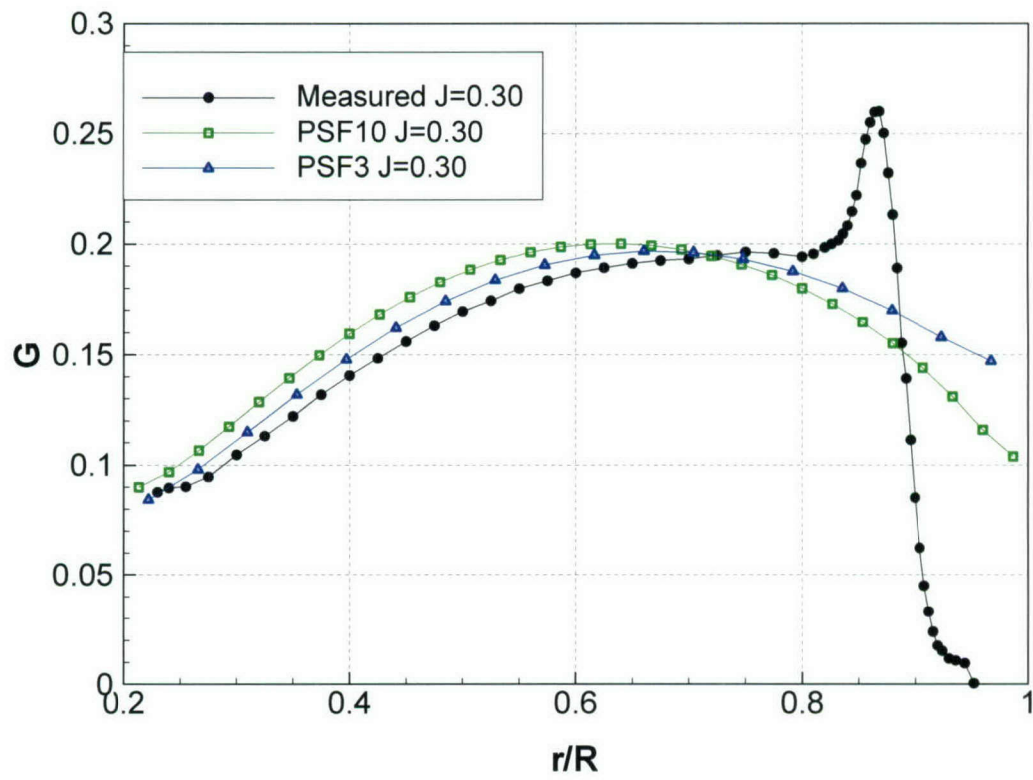


**Figure 20. Spanwise Circulation at  $J = +0.3$**

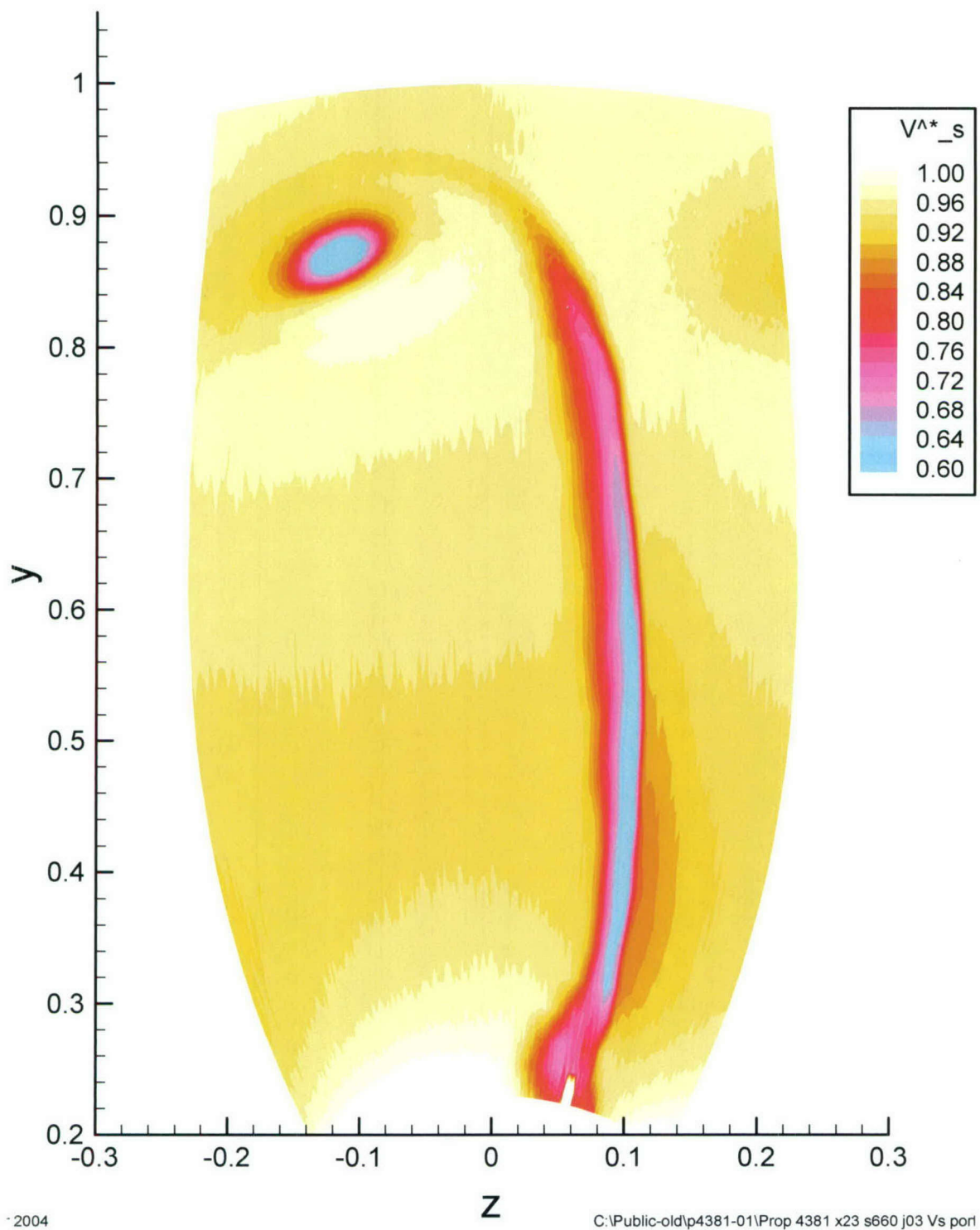


**Figure 21. Streamwise Velocity for P4381 from LDV at  $J = +0.3$ ,  $x = +0.23$**

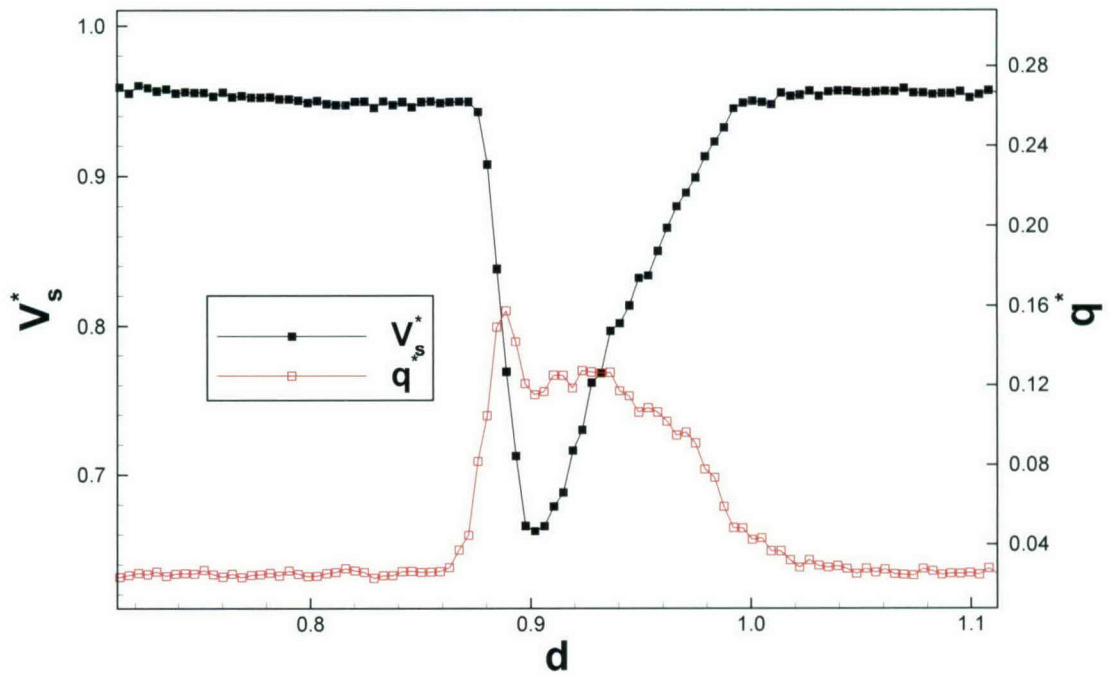


Figure 22. Blade Wake from LDV at  $J = +0.3$ ,  $x = 0.7$

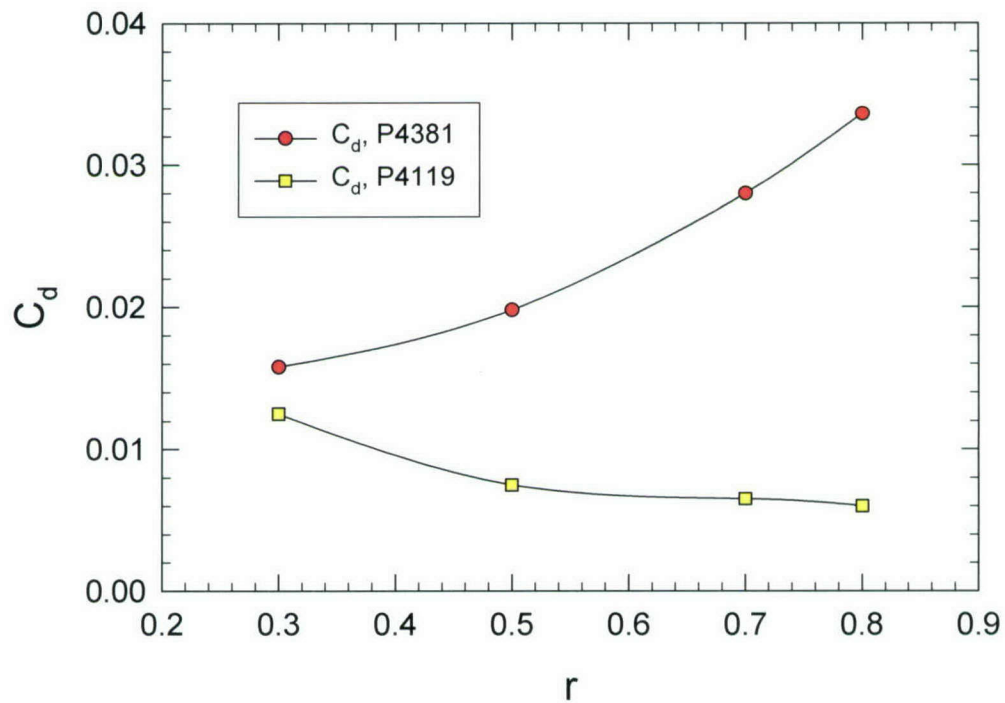
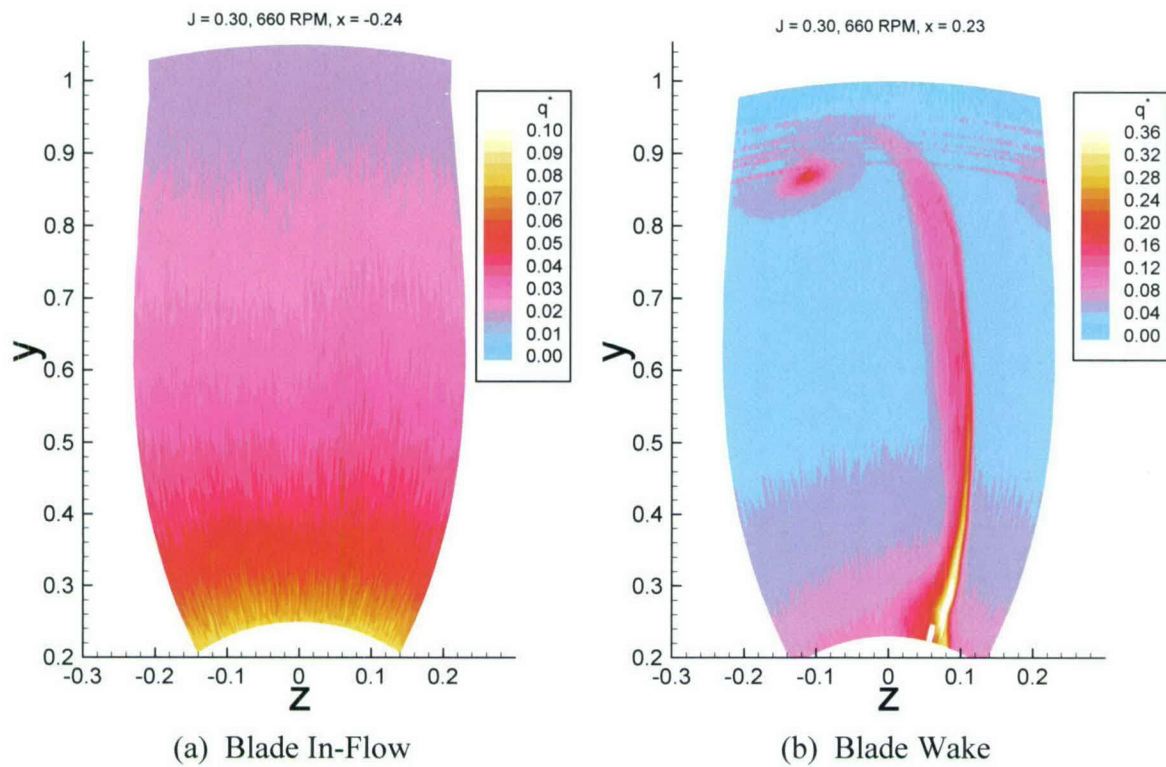
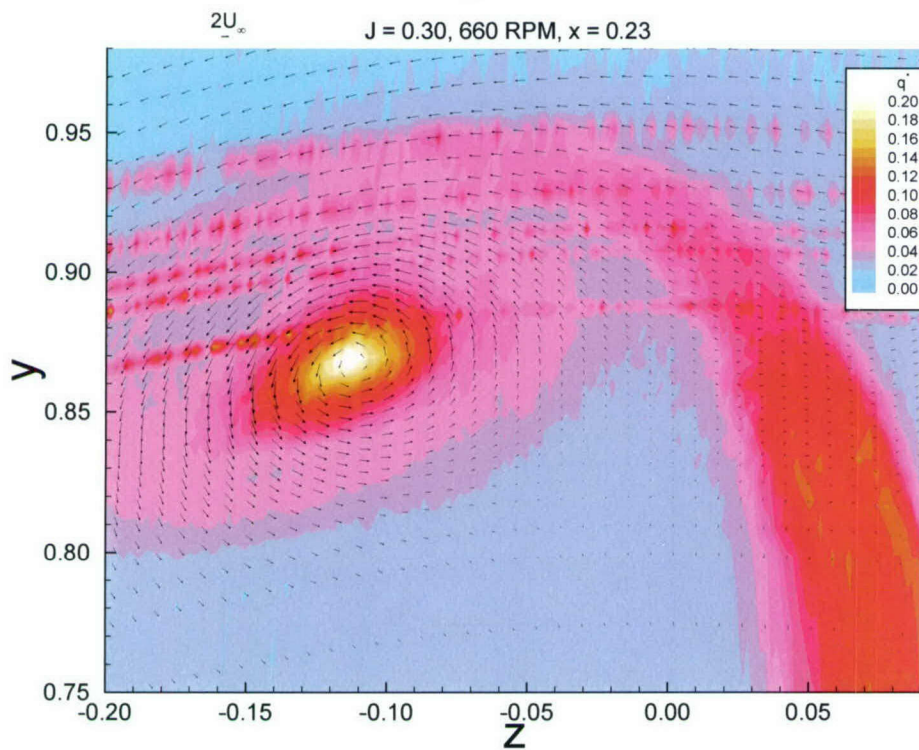


Figure 23. Computed Drag Coefficients for P3381 at  $J = +0.3$  & P4119,  $J_{des} = 0.83$



**Figure 24. Local Total Kinetic Energy in Ahead for Propeller 4381 at  $J = +0.3$**



**Figure 25. Detail of Tip Vortex in Ahead at  $J = +0.3$**

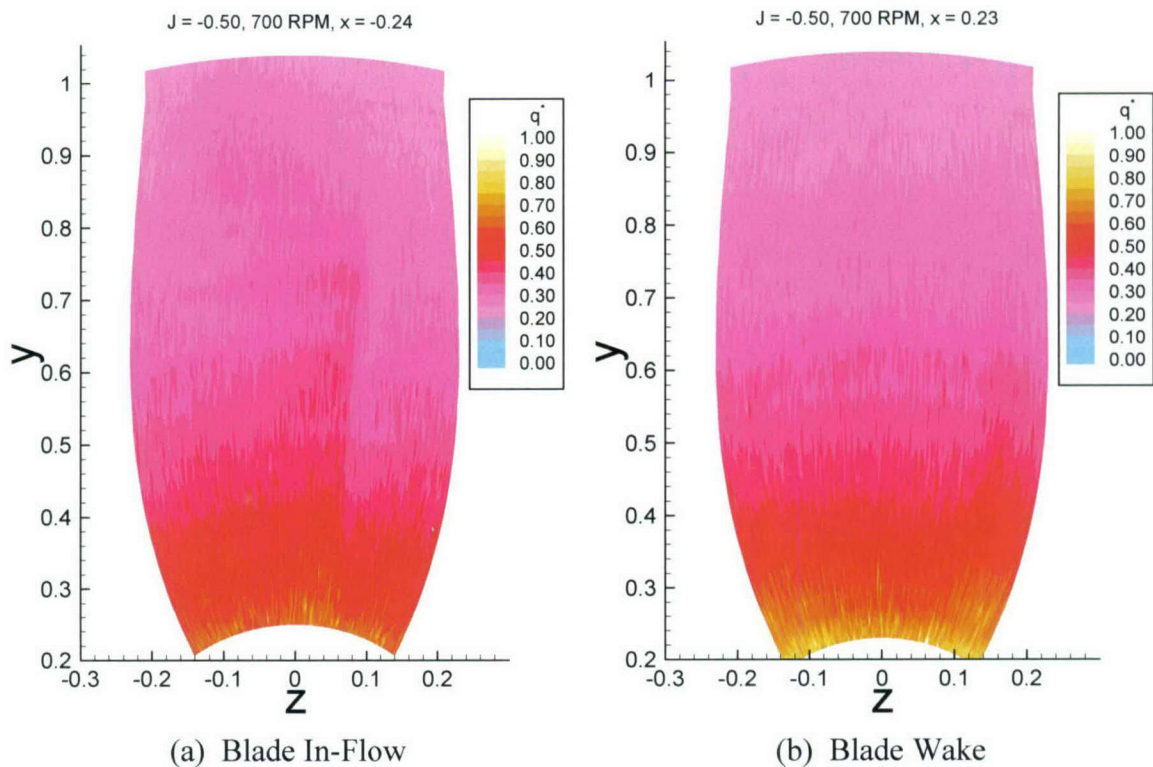


**Figure 26. Local Total Kinetic Energy in Crashback for Prop 4381 at  $J = -0.5$**

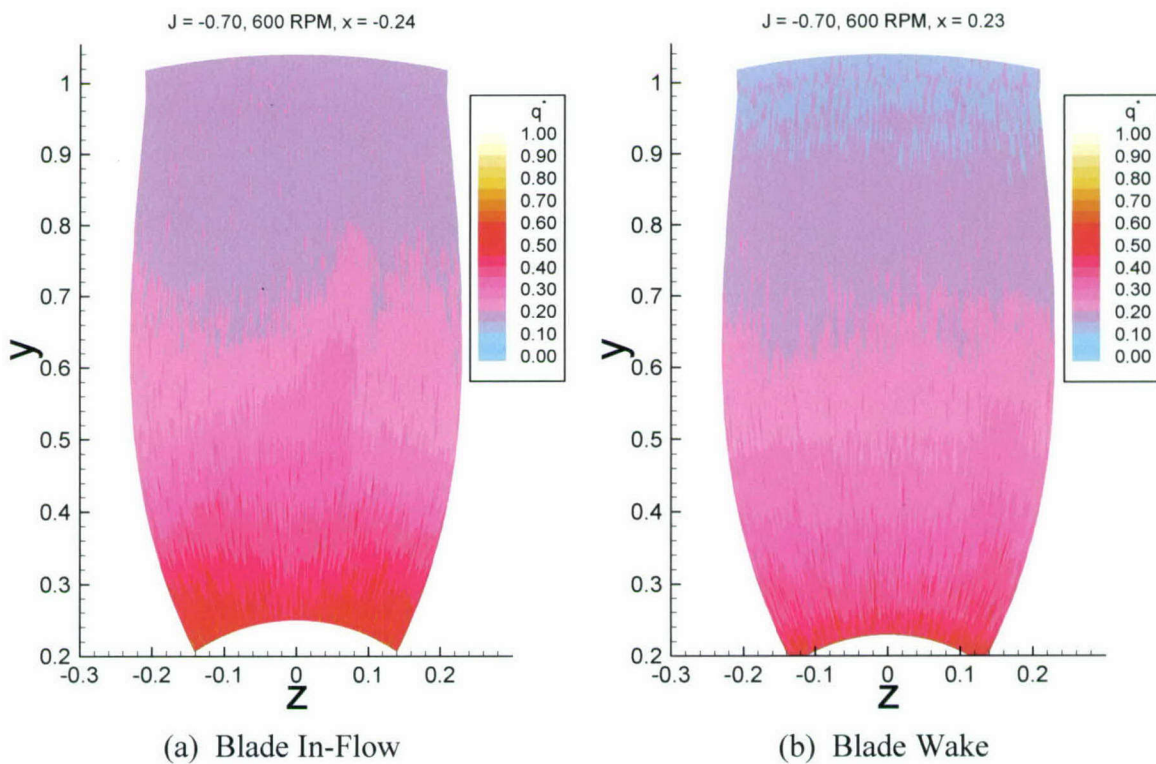


**Figure 27. Local Total Kinetic Energy in Crashback for Prop 4381 at  $J = -0.7$**

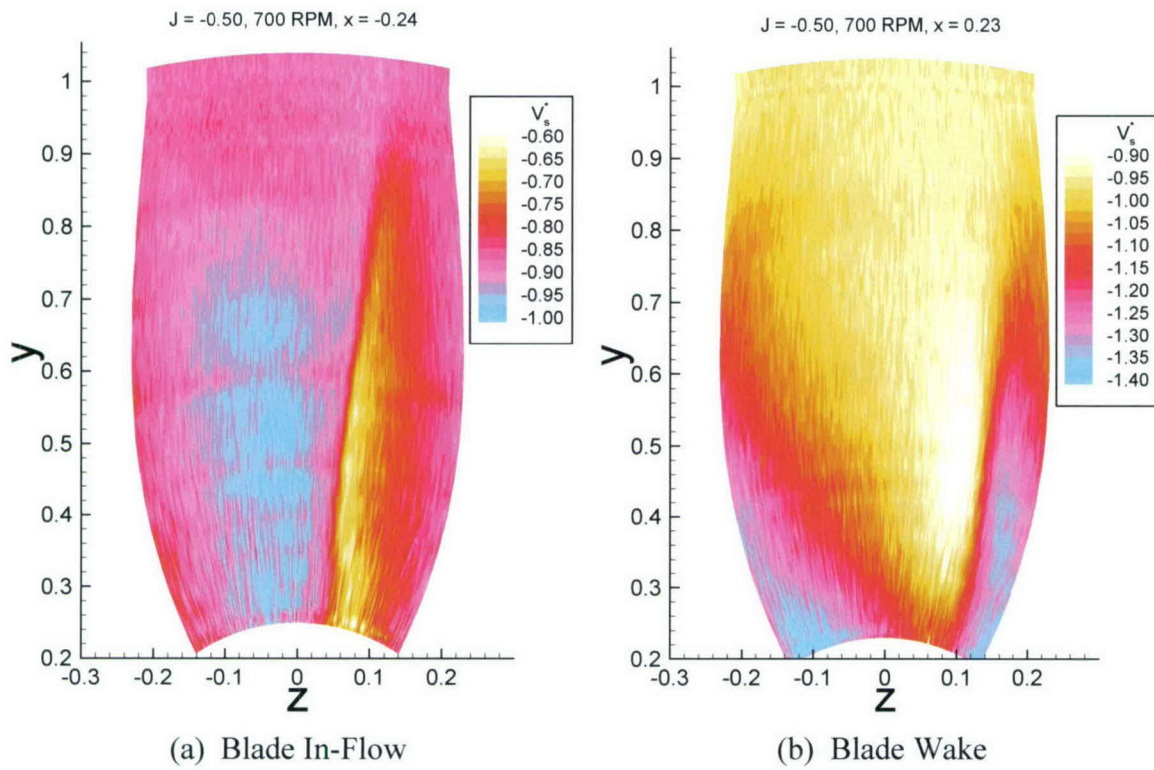


**Figure 28. Streamwise Velocity in Crashback for Prop 4381 at  $J = -0.5$**

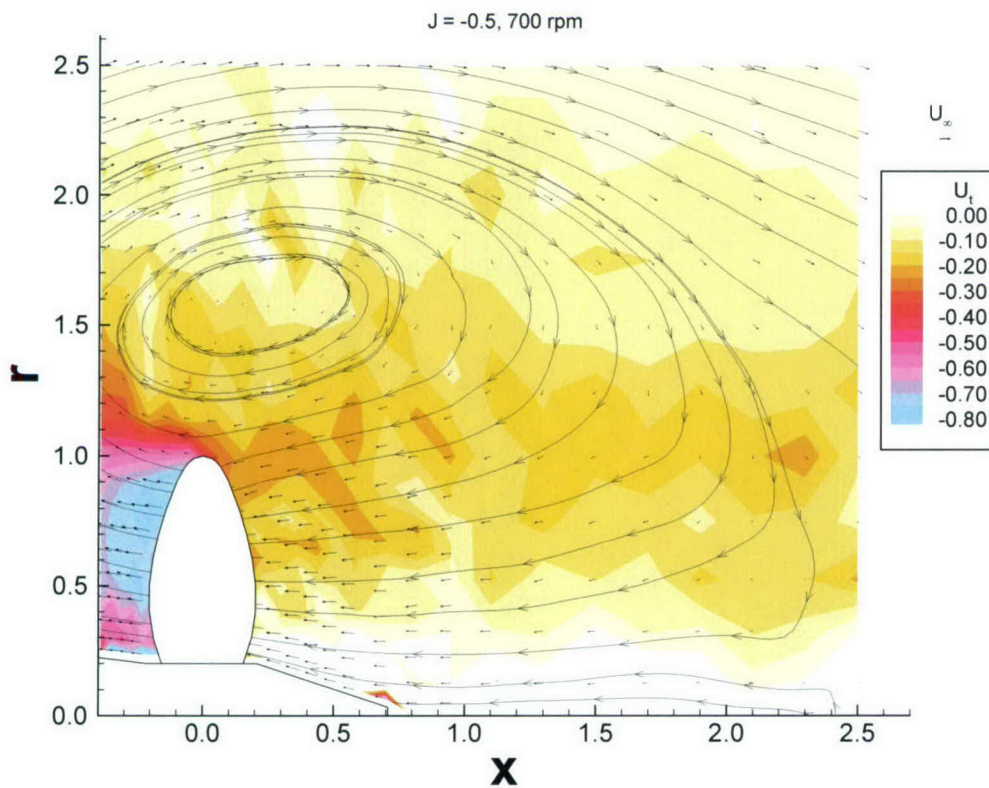


**Figure 29. Mean Velocity Components in Crashback at  $J = -0.5$**

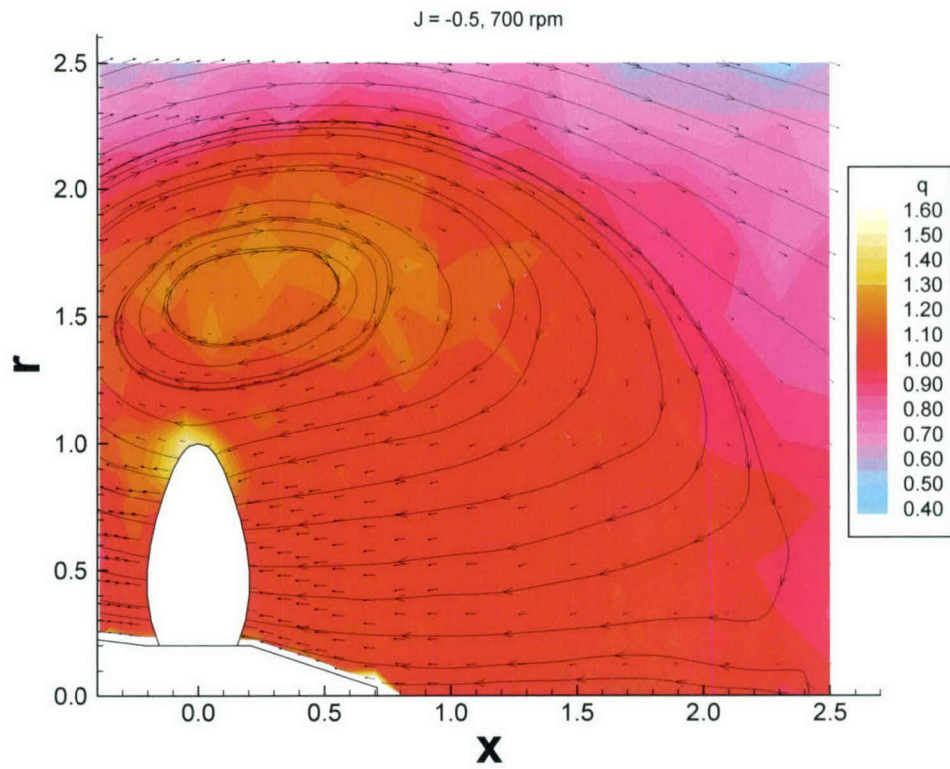


**Figure 30. X-R Plane Total Kinetic Energy in Crashback at  $J = -0.5$**

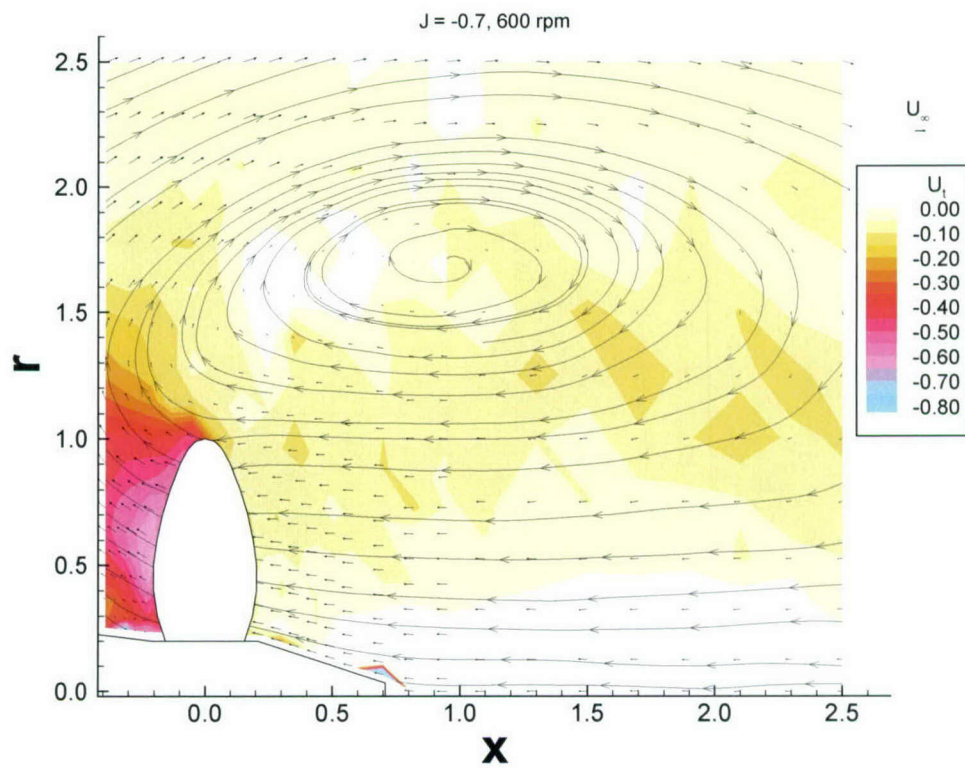


**Figure 31. Mean Velocity Components in Crashback at  $J = -0.7$**

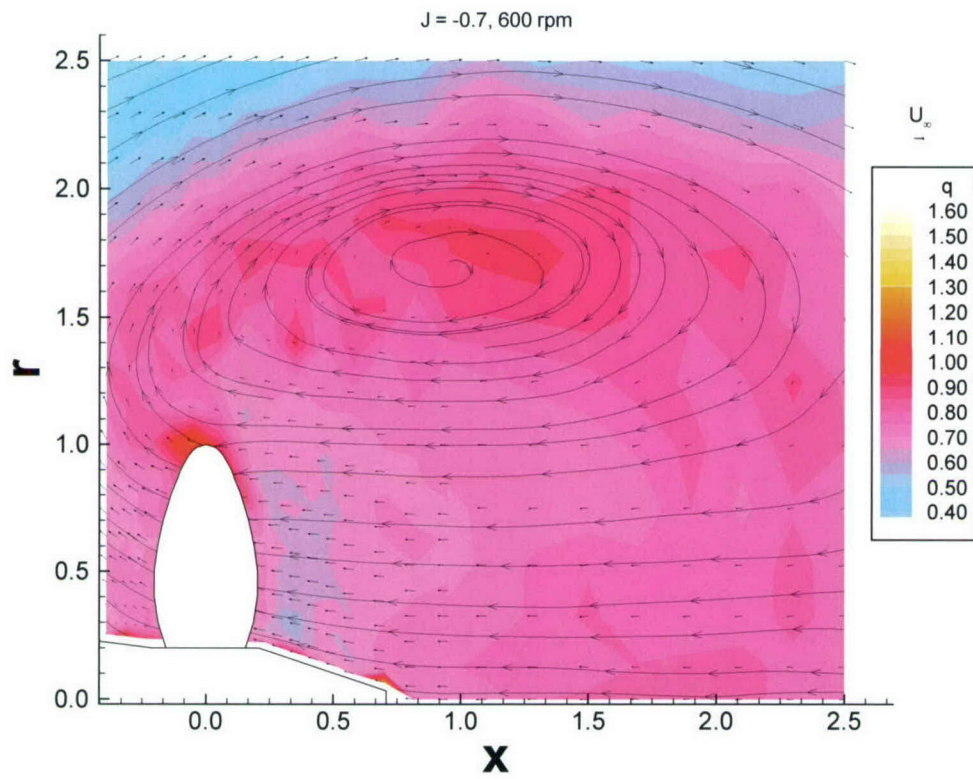
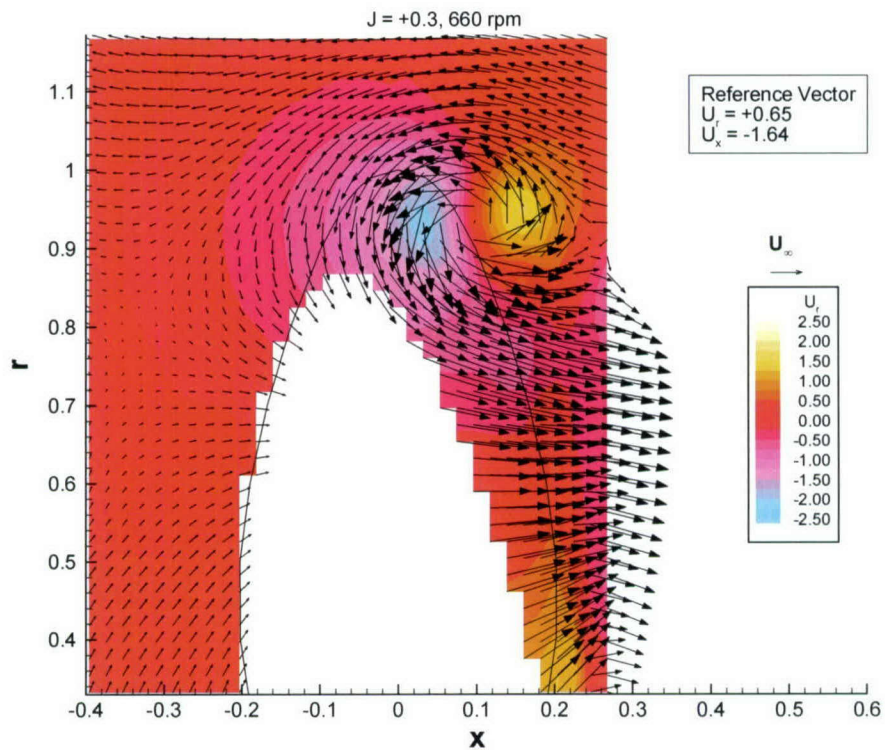
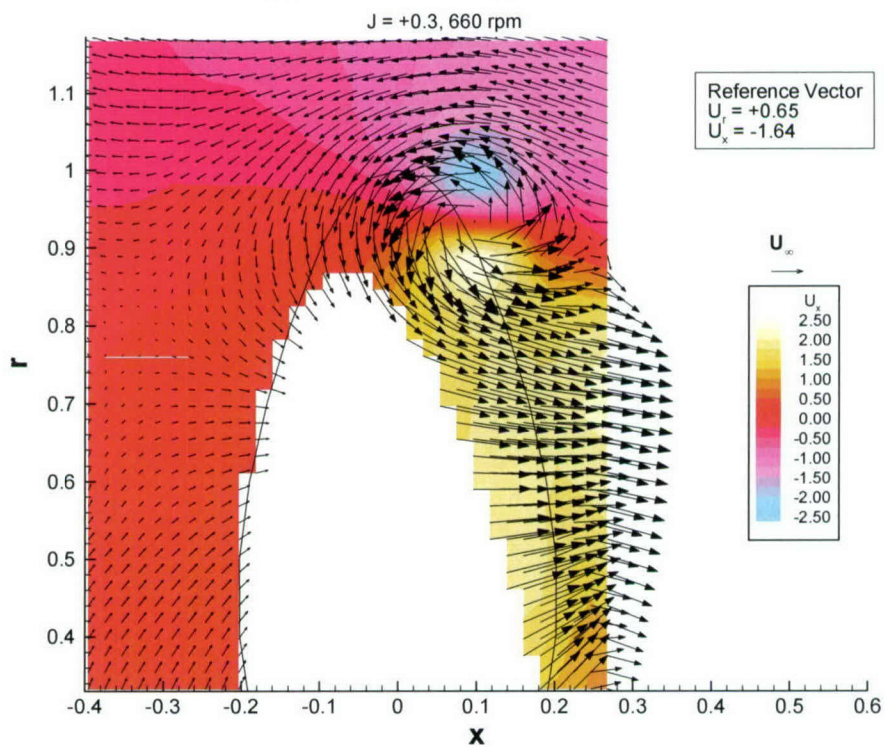


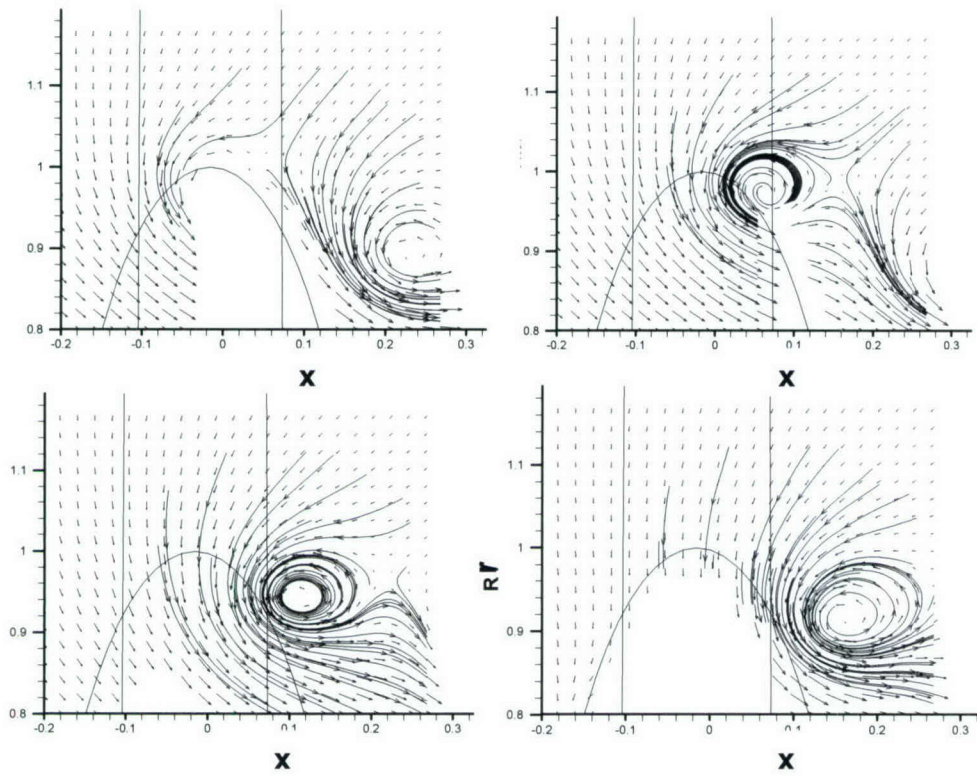
**Figure 32. X-R Plane Total Kinetic Energy in Crashback at  $J = -0.7$**



(a) Radial Velocity Contour Plot



(b) Axial Velocity Contour Plot



(c) Tip Flow Streamlines, Time Average Images 18° Apart

**Figure 33. Averaged Relative Velocities of Tip Vortex from PIV at  $J = +0.3$**

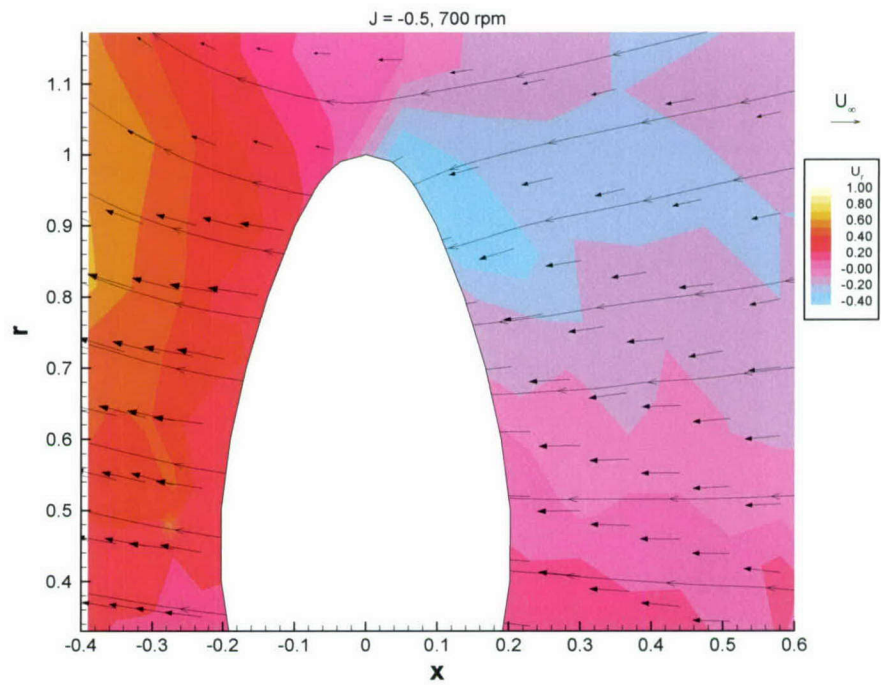
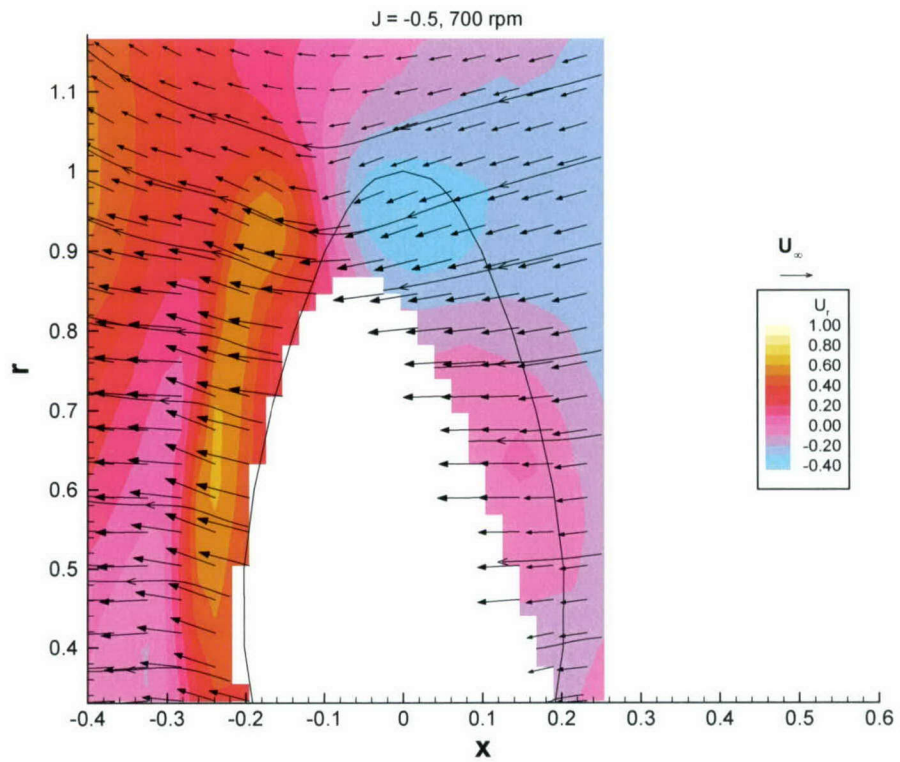
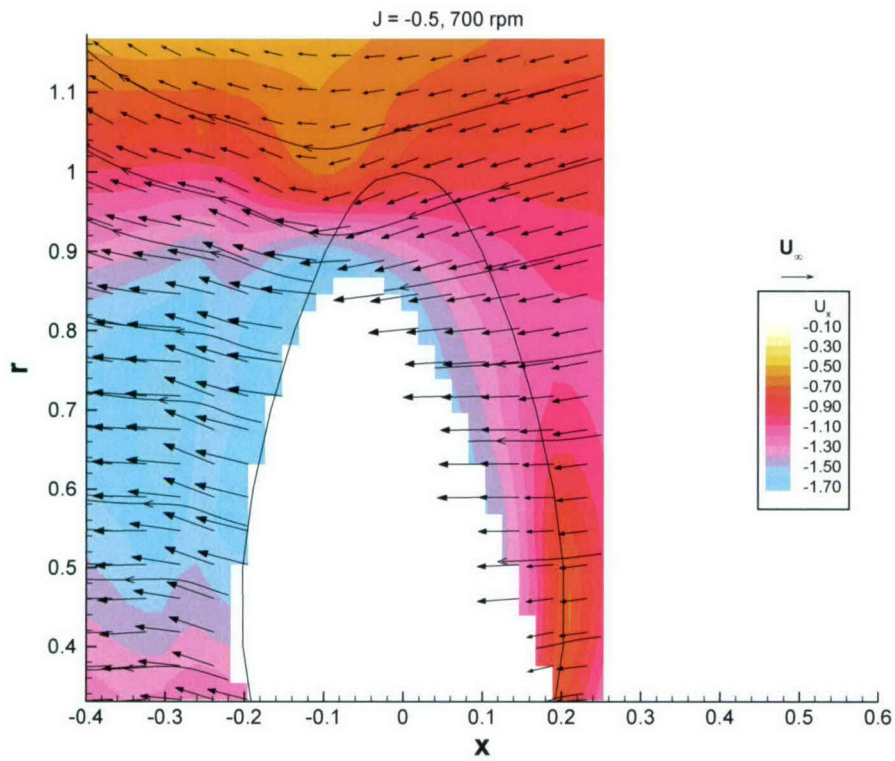
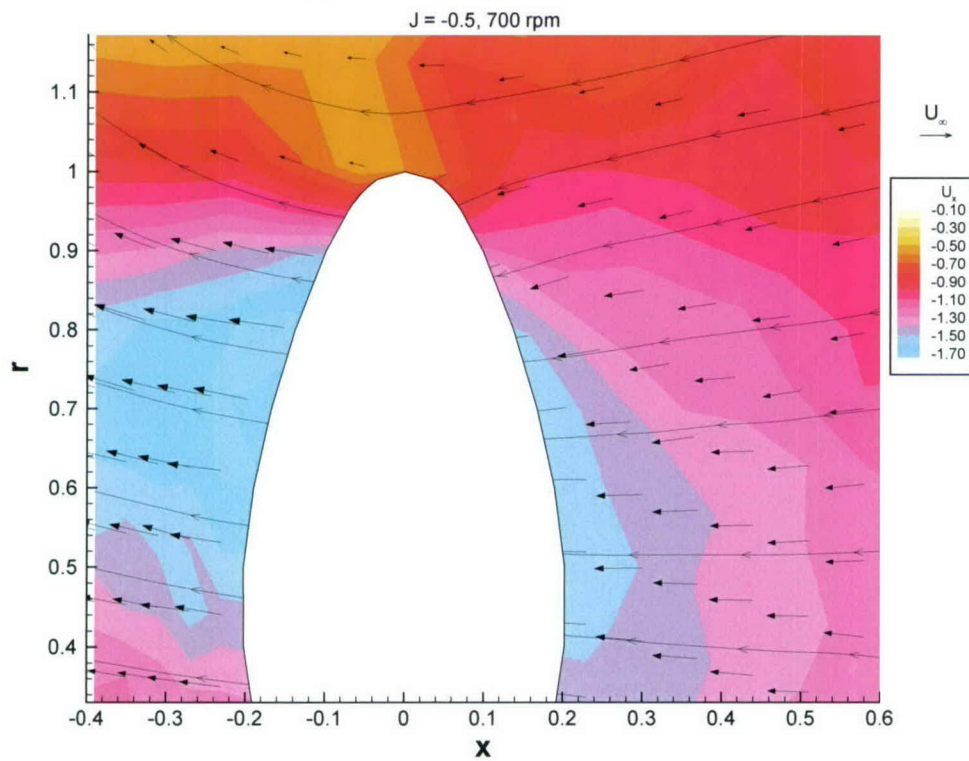


**Figure 34. Comparison of PIV and LDV Radial Velocity in Crashback at  $J = -0.5$**

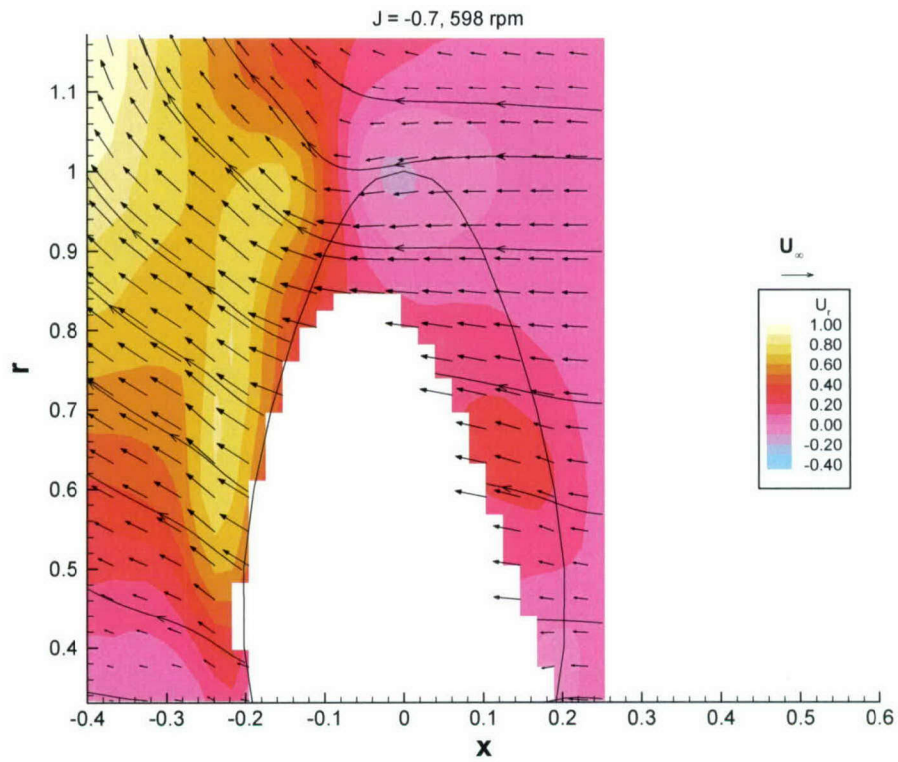


(a) PIV Averaged Data

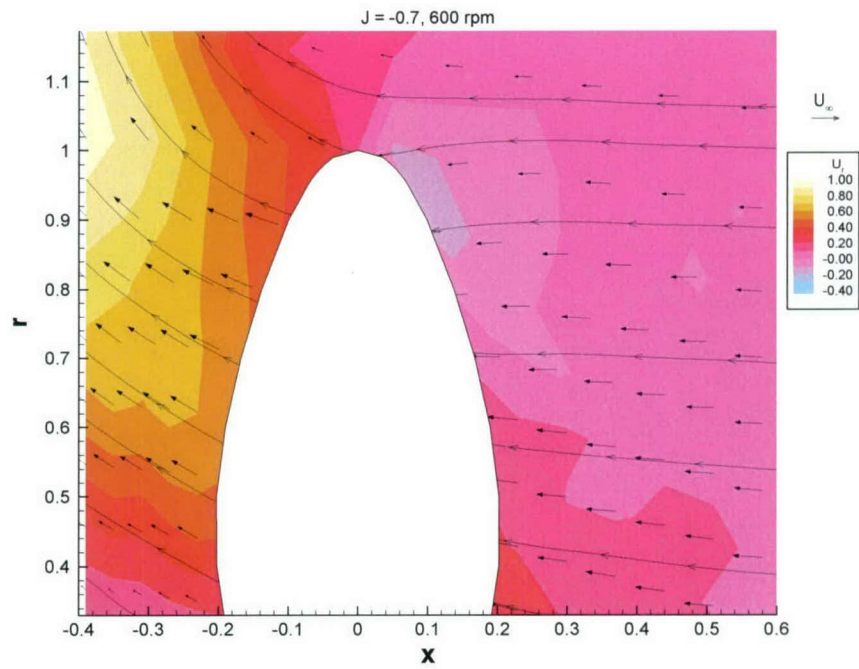


(b) LDV Data

**Figure 35. Comparison of PIV and LDV Axial Velocity in Crashback at  $J = -0.5$**

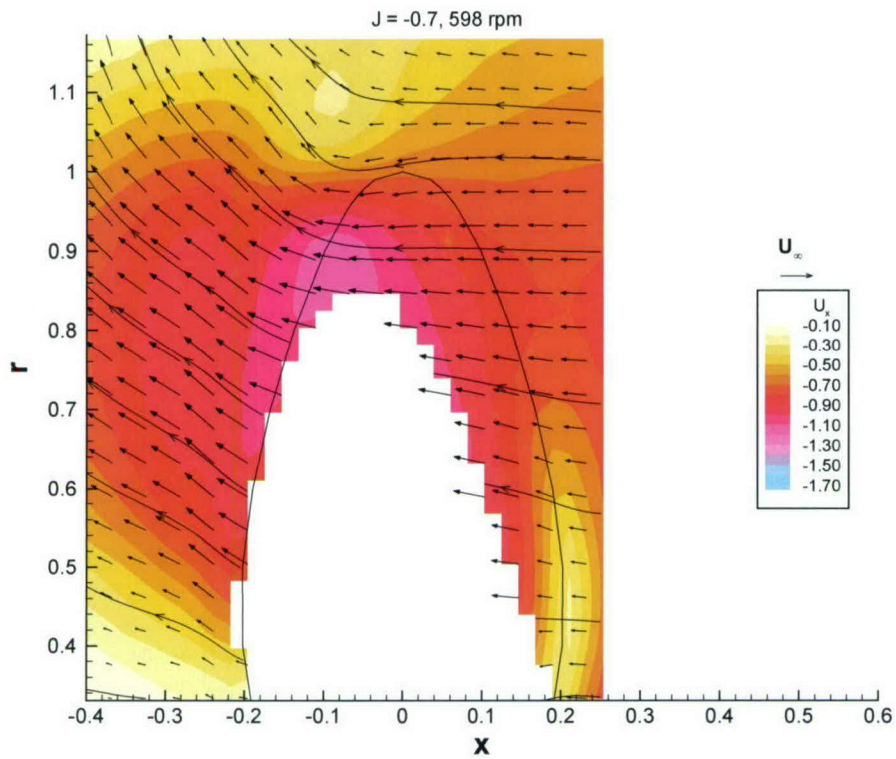


(a) PIV Averaged Data

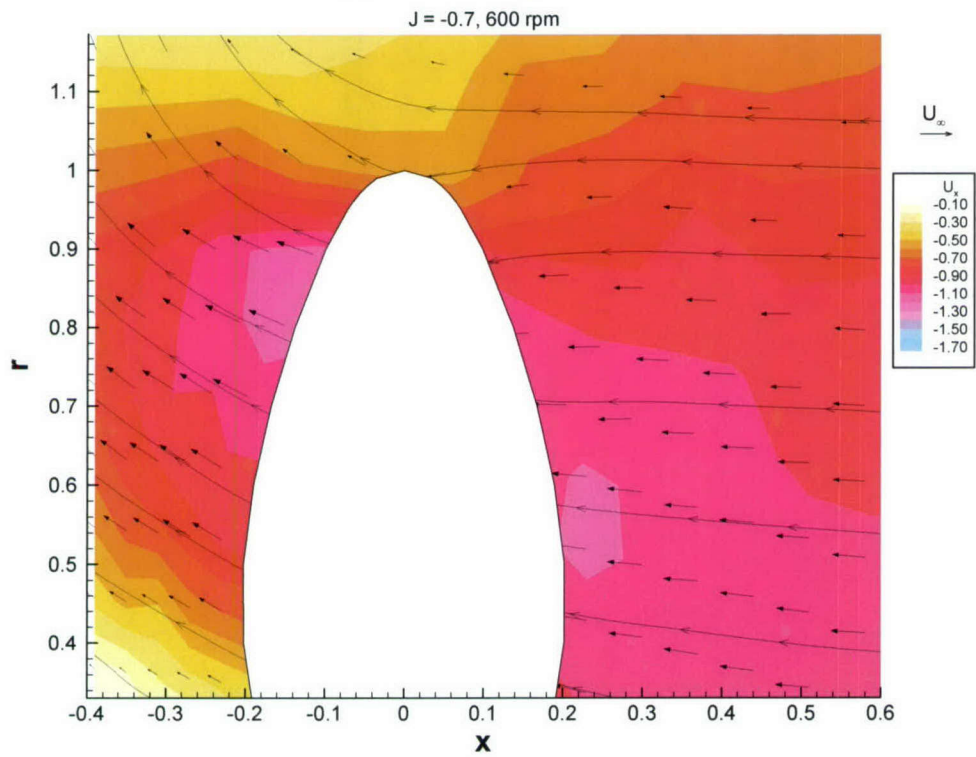


(b) LDV Data

**Figure 36. Comparison of PIV and LDV Radial Velocity in Crashback at  $J = -0.7$**



(a) PIV Averaged Data



(b) LDV Data

**Figure 37. Comparison of PIV and LDV Axial Velocity in Crashback at  $J = -0.7$**

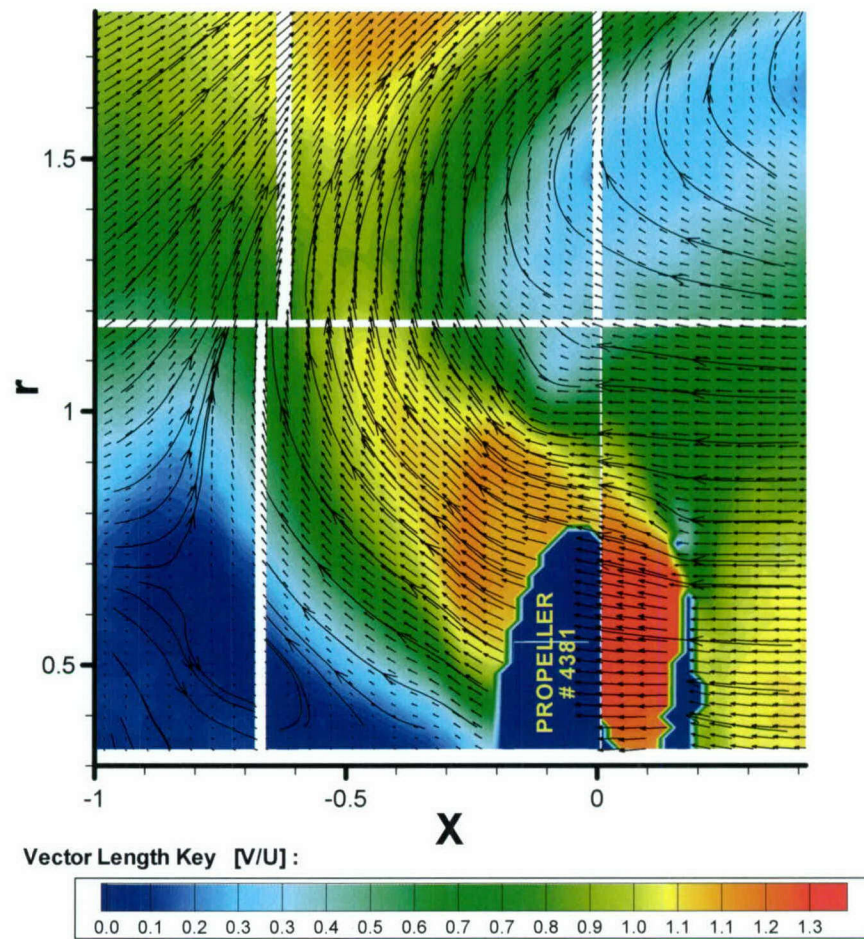
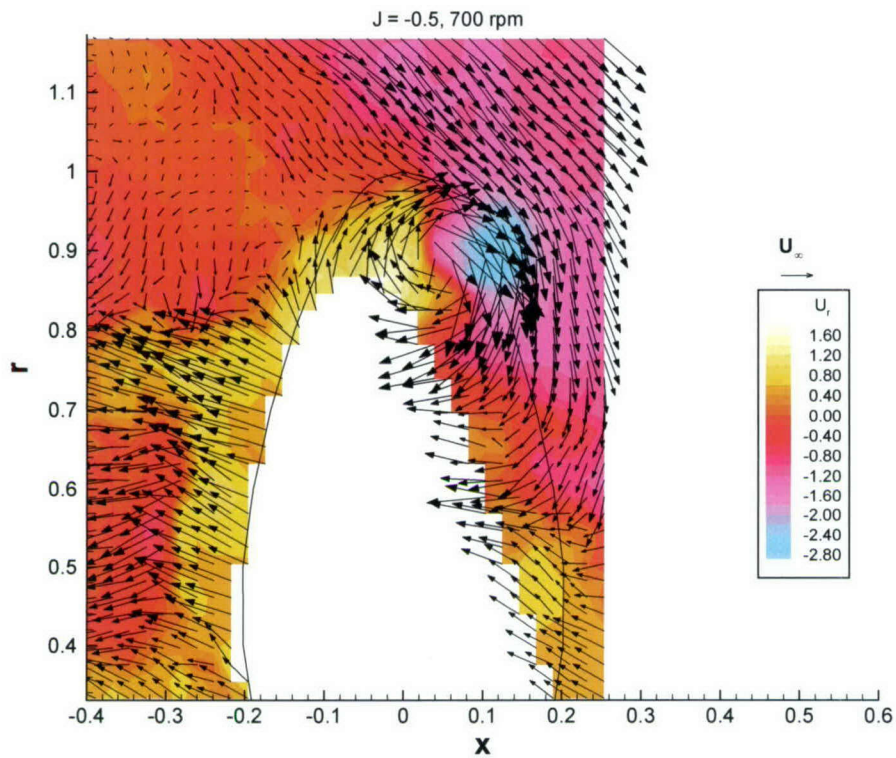
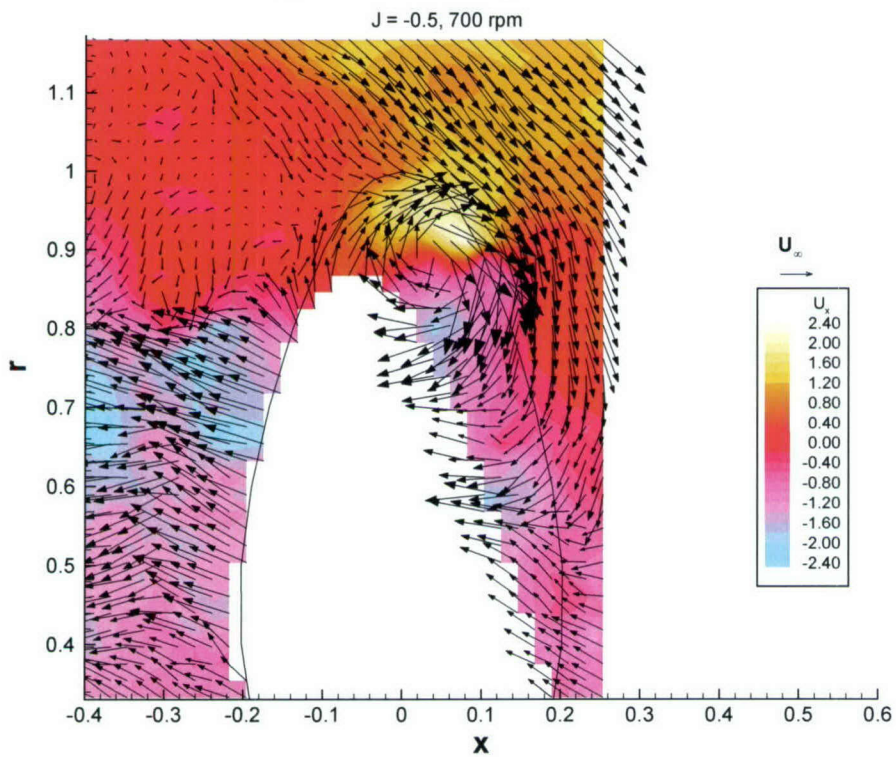


**Figure 38. Average Streamline Velocity from Mosaic of 6 PIV Images at  $J = -0.7$**

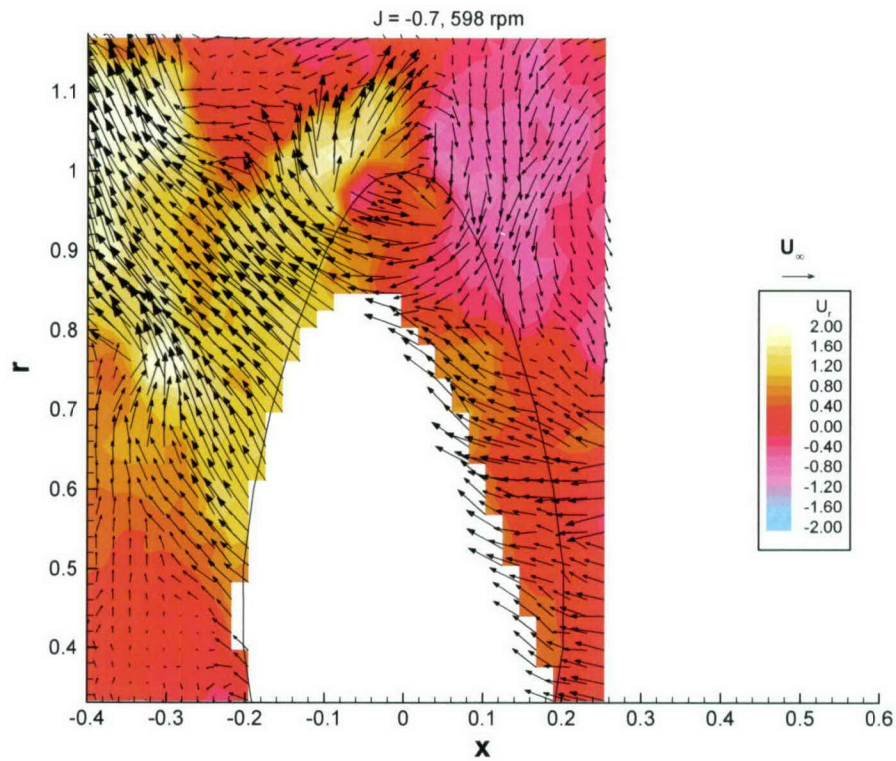


(a) Radial Velocity Contour Plot

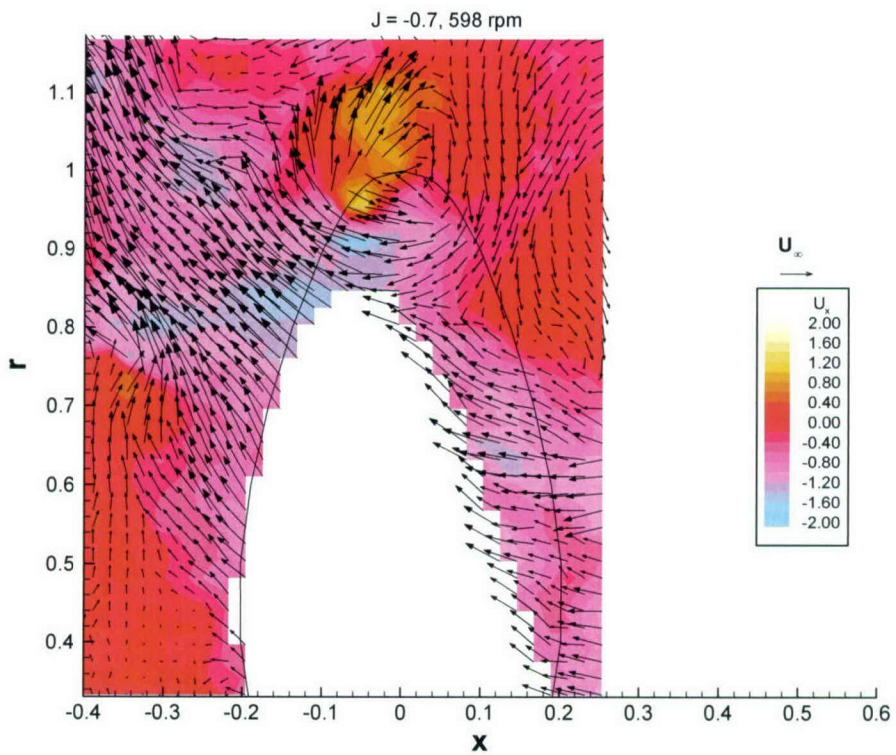


(b) Axial Velocity Contour Plot

**Figure 39. Instantaneous Velocity Vectors from PIV in Crashback at  $J = -0.5$**

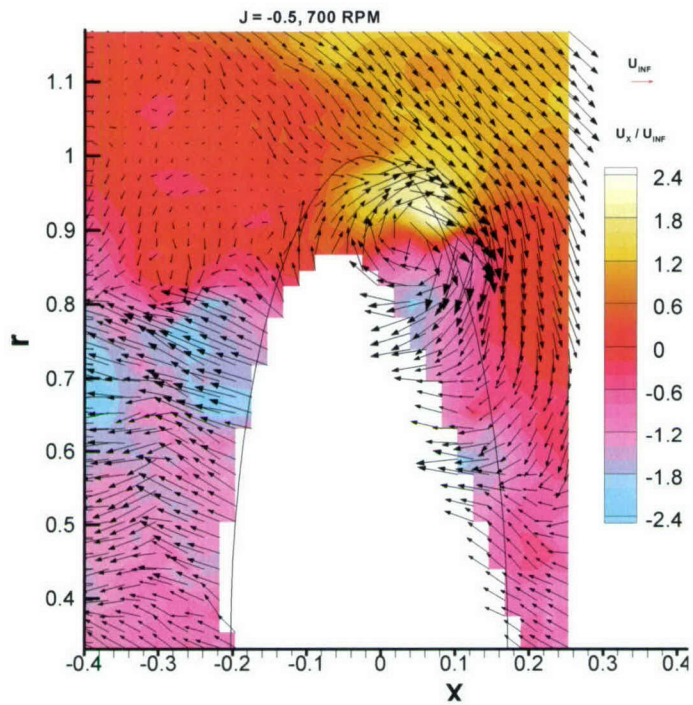


(a) Radial Velocity Contour Plot

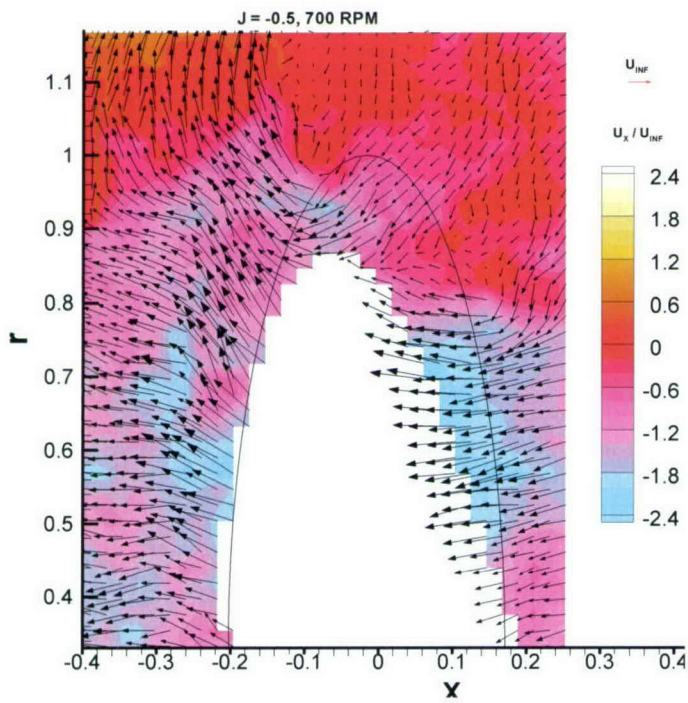


(b) Axial Velocity Contour Plot

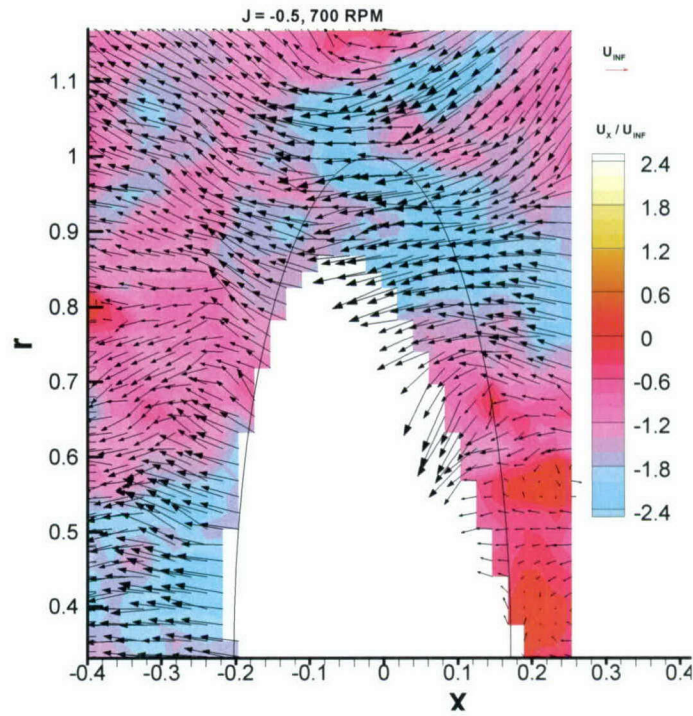
**Figure 40. Instantaneous Velocity Vectors from PIV in Crashback at  $J = -0.7$**



(a) Most extreme of 1000



(b) 8<sup>th</sup> extreme of 1000



(c) Best of 1000

Figure 41. Instantaneous Axial Velocity and Streamlines from PIV at  $J = -0.5$

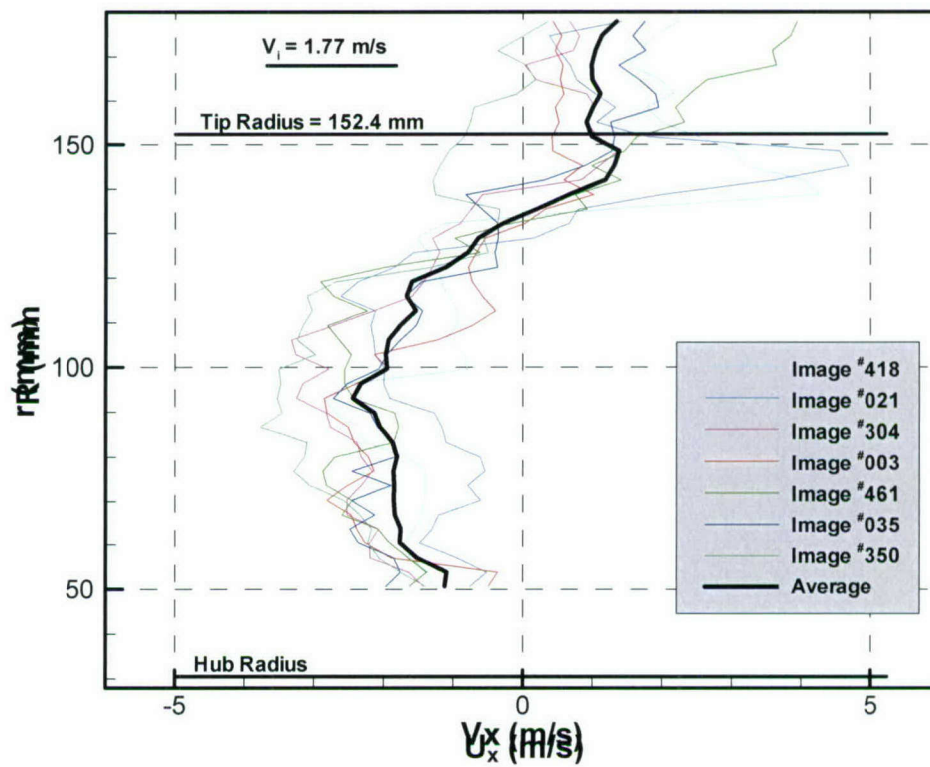
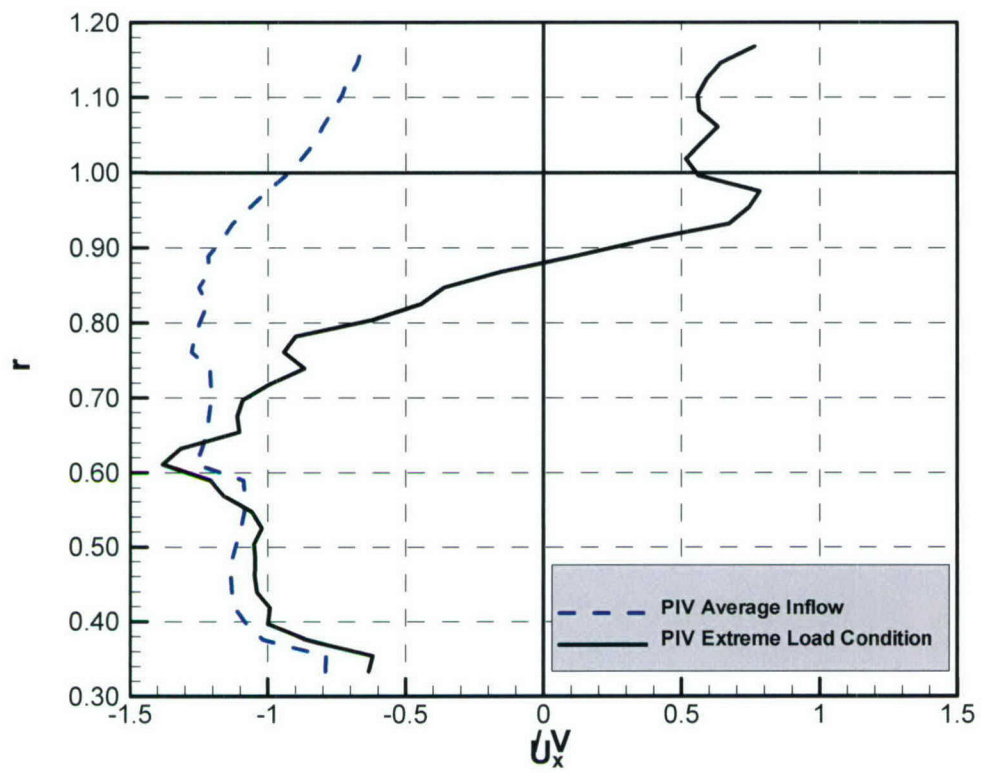


Figure 42. Eight Most Extreme Propeller Inflow Axial Velocity Data



**Figure 43. Average and “Extreme” Propeller 4381 Inflow from at  $J = -0.5$**

This page intentionally left blank.

**Table 1. Geometric Characteristics of Propeller 4381**

Diameter ( $D$ ) =	305 mm (12 inches)
Number of Blades ( $Z$ ) =	5
Rotation	Right Handed
Expanded Area Ratio =	0.725
Camber Distribution =	NACA a=0.8 mean line
Thickness Distribution =	NACA 66 (TMB modified)

$r$	$C/D$	$t/C$	$f/C$	$P/D$	$\theta_s$ (deg)	$i/D$
0.200	0.1735	0.0868	0.01084	1.2648	0.00	0.00
0.300	0.2283	0.0714	0.01684	1.3450	0.00	0.00
0.400	0.2750	0.0588	0.01916	1.3583	0.00	0.00
0.500	0.3125	0.0480	0.01916	1.3358	0.00	0.00
0.600	0.3375	0.0382	0.01650	1.2800	0.00	0.00
0.700	0.3475	0.0292	0.01316	1.2100	0.00	0.00
0.800	0.3342	0.0210	0.00984	1.1367	0.00	0.00
0.900	0.2808	0.0134	0.00684	1.0658	0.00	0.00
0.950	0.2192	0.0116	0.00584	1.0329	0.00	0.00
0.960	0.2021	0.0112	0.00550	1.0264	0.00	0.00
0.970	0.1800	0.0110	0.00516	1.0200	0.00	0.00
0.980	0.1521	0.0112	0.00500	1.0138	0.00	0.00
0.990	0.1146	0.0114	0.00484	1.0075	0.00	0.00
1.000	0.0000	0.0000	0.00000	1.0013	0.00	0.00

**Table 2. Elemental Uncertainties for LDV Measurements**

Item	Type B	Type A
$U_\infty$	0.005	0.003
$n$	0.00008	0.00014
$d_f$	0.003	
$x$	0.0005	
$t, r$	0.0010	
$\theta$		0.05°

**Table 3. Calculated Uncertainties for LDV Measurements**

Item	Case 1 (Inviscid Flow)			Case 2 (Propeller Wake)			Reference
	Type B	Type A	Total	Type B	Type A	Total	
$J$	0.005	0.003	0.006	0.005	0.003	0.006	$J$
$U_x, V_x$	0.003	0.002	0.004	0.003	0.03	0.03	$U_\infty$
$U_t$	0.001	0.001	0.002	0.002	0.015	0.015	$U_\infty$
$U_r, V_r$	0.0003	0.001	0.001	0.001	0.03	0.023	$U_\infty$
$V_t$	0.001	0.001	0.002	0.002	0.015	0.015	$U_\infty$
$V_s$	0.002	0.002	0.003	0.002	0.02	0.019	$U_\infty$
$V_c, V_p$	0.003	0.002	0.004	0.003	0.03	0.028	$U_\infty$
$q$	0.00	0.10	0.10	0.00	0.10	0.10	$q$

**Table 4. Test Conditions**

J	n (rpm)	$U_\infty$ (m/s)	$U_\infty$ (ft/s)
+0.3	660	1.006	3.30
-0.5	-700	1.778	5.83
-0.7	-600	2.134	7.00

**Table 5. Thrust and Torque Predictions at J = +0.3**

	$K_T$	$10K_Q$	$\eta$
PSF10, Cd = 0.007	0.507	0.759	0.319
PSF10, Cd, meas	0.495	0.857	0.275
Water Tunnel	0.432	0.747	0.274
Tow tank	0.469	0.789	0.284

**Table 6. Comparison of Propulsion and Flow Statistics**

J	$\sigma_T/T1$	$\sigma_Q/Q1$	q	$Re/10^5$
+0.3	0.019	0.008	---	8.4
-0.5	0.249	0.231	1.52	8.9
-0.7	0.175	0.176	1.13	7.8

Note: Maximum values of q near blade tip

## References

- [1] Jiang, C. W., Dong, R. R., Liu, H. L., and Chang, M. S., 1996. "24-inch Water Tunnel Flow Field Measurements during Propeller Crashback," Proceedings of the 21<sup>st</sup> ONR Symposium on Naval Hydrodynamics, Tondheim, Norway, pp. 136-146.
- [2] Chen, B., 1996. "Computational Fluid Dynamics of Four-Quadrant Marine Propeller Flow," Master of Science Thesis, The University of Iowa, Iowa City, Iowa.
- [3] Davoudzadeh, F., Taylor, L. K., Zierke, W. C., Dreyer, J. J., McDonald, H., and Whitfield, D. L., 1997. "Coupled Navier-Stokes and Equations of Motion Simulation of Submarine Maneuvers, Including Crashback," Paper FEDSM97-3129, Fluids Engineering Division Summer Meeting, The American Society of Mechanical Engineers (ASME), Vancouver, British Columbia.
- [4] ISO, 1995. "Guide to the Expression of Uncertainty in Measurement," International Organization for Standardization, Geneva, Switzerland.
- [5] Bendat, Julius S., and Piersol, Allan G, 1971. ***Random Data: Analysis and Measurement Procedures***, New York: Wiley-Interscience, pp. 219-233.
- [6] Jessup, S. D., 1989. An Experimental Investigation of the Viscous Aspects of Propeller Blade Flow," Ph.D. Thesis, The Catholic University of America.
- [7] Townsend, A. A., 1976. ***The Structure of Turbulent Shear Flow***, Second Edition, Cambridge, Cambridge University Press, p. 208.
- [8] Jiang, C.W., Dong, R.R., Liu, H.L. and Chang, M.S., 1996. "24-inch Water Tunnel flow Field Measurements During Propeller Crashback," 21<sup>st</sup> ONR Symposium on Naval Hydrodynamics, Trondheim, Norway, pp. 136-146.

This page intentionally left blank.

**Distribution**

	<i>Copies</i>			<i>Copies</i>
Dr. Ronald D. Joslin	1	<b>NSWC, CARDEROCK DIVISION INTERNAL</b>		
Office of Naval Research, Code 333		<b>DISTRIBUTION</b>		
800 North Quincy Street		Code Name		
Arlington, VA 22217-5660 USA				
Dr. Ki-Han Kim	3	5000 I. Y. Koh		1
Office of Naval Research, Code 333		5010 C. C. Burdette		1
800 North Quincy Street		5060 D. A. Walden		1
Arlington, VA 22217-5660 USA		5080 J. F. Brown		1
		5200 W. G. Day, Jr.		1
Dr. L. Patrick Purtell	3	5400 S. D. Black		1
Office of Naval Research, Code 333		C. J. Chesnakas		3
800 North Quincy Street		M. J. Donnelly		3
Arlington, VA 22217-5660 USA		D. J. Fry		3
		J. J. Gorski		1
DTIC	1	S. D. Jessup		3
		J. T. Park		3
		R. P. Szwerc		1
		5600 E. S. Ammeen		1
		K. A. Junghans		1
		P. Atsavapranee		1
		7051 W. K. Blake		1
		Library		2

This page intentionally left blank.

